I.FAST

Innovation Fostering in Accelerator Science and Technology

Horizon 2020 Research Infrastructures GA n° 101004730

DELIVERABLE REPORT

Manufacturing and testing of two beam-windows prototypes

DELIVERABLE: D4.3

Document identifier:	IFAST-D4.3
Due date of deliverable:	End of Month 38 (June 2024)
Report release date:	03/06/2024
Work package:	WP4:
Lead beneficiary:	CERN
Document status:	Final

ABSTRACT

Task 3 within WP4 researches materials and assembling techniques for particle beam windows. In particle accelerators, a beam window is a device which separates environment at different pressures. Typical example is the beam windows in transfer lines, which separate atmospheric pressure from the beam vacuum. Such systems are complex, because they must possess thermal transfer properties and mechanical resistance; moreover, they must be radiation-hard, maintaining such properties over time under the effect of ionizing radiation.

In the scope of this deliverable, the team produced and tested under beam four beam windows assemblies, of different materials, characterizing their microstructure and properties before and after irradiation. The irradiation took place at the CERN IRRAD facilityin September-October 2023, and the post-irradiation examination, after enough cooldown, was completed in May 2024. This document summarizes the main achievements and the results obtained.

For more information on IFAST, its partners and contributors please see https://ifast-project.eu/

This project has received funding from the European Union's Horizon 2020 Research and Innovation programme under Grant Agreement No 101004730. IFAST began in May 2021 and will run for 4 years.

Delivery Slip

	Name	Partner	Date
Authored by	F. Carra, S. Marin, F. Salvat-Pujol, J. Swieszek, M. Tomut, N. Vejnovic C. Belei, M. Kitzmantel	CERN, RHP	31/05/2024
Reviewed by	M. Vretenar [on behalf of Steering Committee]	CERN	03/06/2024
Approved by	Steering Committee		03/06/2024

TABLE OF CONTENTS

Executive summary

This document summarizes the results of the deliverable D4.3 of WP4, consisting in the production and irradiation of four beam windows assemblies of different constitutive materials. The document also contains the results of the post-irradiation examination performed at CERN in April/May 2024.

Chapter 1 gives a context to the research work, and summarizes the objective of the project, and of the specific deliverable.

Chapter 2 illustrates the beam windows assemblies produced at RHP, their properties and geometrical parameters, as well as the production technique.

Chapter 3 focuses on the configuration of the irradiation parameters at the CERN IRRAD facility, including the dose and fluence on the samples and the produced Displacements-Per-Atom (DPA) and gas nucleation in each sample.

Chapter 4 is dedicated to the pre- and post- irradiation characterization of the assemblies, summarizing the main results in terms of macro and microstructure, electrical and thermal conductivity.

Chapter 5 summarizes the main conclusions and the future plans of the task WP4.3.

1 Introduction

A beam vacuum window is a thin interface of separation between a volume under vacuum and a volume at higher pressure traversed by particle beams. Their application is not limited to particle accelerators, where they are typically installed inside the beamline to separate vacuum sectors, but also extends to other fields of nuclear research and to high-power hadron beam applications, such as the Spallation Neutron Sources (SNS) and the Accelerator-driven systems (ADS) [1].

Figure 1: Beryllium beam window for NuMI beamline, Fermilab [2].

The research and development of innovative materials and designs capable of withstanding higher pressure loads and more severe beam-induced thermal stresses has become extremely relevant, as

the energy and pulse intensities of new accelerator facilities have increased. Another critical requirement is the safe operation of future facilities, as well as the prevention of failures resulting from radiation damage and the combined effect of pressure waves and thermal stresses [3]. In this respect, IFAST WP4 “Managing Innovation: Beam Windows and Composite Materials” dedicates a task, WP4.3, to the study and development of beam windows. WP4 offers a unique platform for this type of study: among its partners, RHP is a company specialized in high-end technology development, and is in charge of the procurement of the beam windows materials, as well as of their assembling on vacuum flanges. GSI offers facilities for the beam irradiation of the targets with ions, as well as expertise on the online and offline characterization. Finally, at CERN, irradiation with protons is possible in a facility named IRRAD [4], and CERN laboratories guarantee extensive characterization of unirradiated and irradiated materials with optical and SEM microscopy, computed micro-tomography, non-destructive techniques (NDT), electrical and thermal conductivity measurement set-ups.

In 2022, a first milestone concerning WP4.3 had already been reached, and submitted to the project coordination [5]. The milestone, named MS13, focused on the production of thin foils of different materials and in their irradiation with ion beams at the GSI M-Branch UNILAC facility. A post-irradiation characterization was also performed, and results led to a consistent scientific production: one master thesis [3], one article approved on international journal [6], a second article submitted and under minor revision, and a third paper under preparation.

In the scope of the deliverable D4.3, the aim of the WP was to move from the production and characterization of thin foils, which are constituting the main element of the beam windows, to the characterization of at least two full windows assemblies. A window assembly consists in a thin foil bonded onto a vacuum flange (see Figure 2). The additional complication here is presented by the bonding technique, which had to be developed ad-hoc at RHP. Also, the bonding process modifies the foil properties, and it is of paramount importance to test under irradiation such “modified” components.

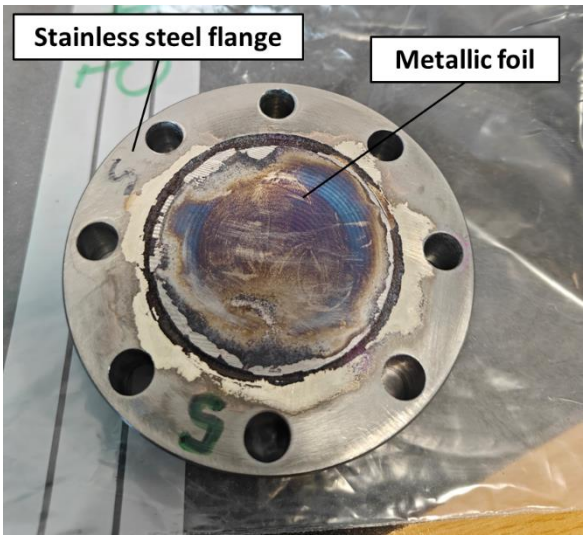

Figure 2: Example of beam window assembly.

For D4.3, due to the unavailability of the GSI irradiation facilities in 2023, an alternative solution was put in place, consisting in irradiating the assemblies at the CERN IRRAD facility. This alternative solution provides the advantage of irradiating the assemblies with a proton beam, instead of with ions. This guarantees a wider spectra of irradiation parameters between MS13 and D4.3, and provides the usual advantages of a proton irradiation. The main advantage is that, at the IRRAD energies (see Chapter 3 for more on this), under proton irradiation, the materials experience the formation of hydrogen and helium. This effects adds up to the Displacement-Per-Atom, both contributing to the material damage. In fact, the presence of hydrogen or helium bubbles at the grain boundaries represents a defect in the crystalline structure. A disadvantage of the proton irradiation is that the samples activation is usually higher, and for this reason we had asked for delaying this D4.3 compared to its initial timeline. In fact, the samples underwent almost six months of cooldown, before reaching doses safe enough for their manipulation at the CERN laboratories.

2 Samples production

Radiation damage on beam windows worsens the thermomechanical properties of the window foil, decreasing its lifetime. Detrimental effects include the fragilization of the foil material and a decrease in thermal conductivity, which hampers its thermal cooldown. Moreover, the bonding of the foil to the vacuum flange can be worsened by radiation damage. Radiation damage, especially in less conventional materials, for which literature is scarce or non-existent, must be evaluated with irradiation tests in facilities such as IRRAD. The change in thermophysical properties after irradiation can then be assessed via post-irradiation examination techniques.

Four beam-window assemblies have been produced at RHP in 2023, and installed in a first sample holder for beam testing at IRRAD. Each beam window assembly is composed of a vacuum flange and a foil (see Figure 2). Table 1 gives the specification of the flange. The same flange is used for all beam window assemblies. The drawing reference for the flange is included in Annex A.1.

Table 1: Flange geometry, mass, and chemical composition

Flange type	Flange material	Int. Diameter (mm)	Ext. Diameter (mm)	Thickness (mm)	Flange weight (g)	Flange chemical composition by weight
Flange for metallic foils	304	50	85	17.5	525.3	Fe 68.9%, Cr 18.5%, Mn 2%, Si 1%, Ni 9.5%, N 0.1%

For the foils, two materials (steel T91 and pure tantalum) in three different thicknesses (0.3 mm, 0.4 mm, and 0.6 mm) were produced, as summarized in Table 2. The reference drawings of the different beam window foils are presented in Annex A.2,3,4,5.

Table 2: Irradiated assemblies – foil mass and chemical composition

Sample number	Foil material	Foil thickness (mm)	Foil weight (g)	Foil chemical composition by weight	Irradiated samples
Sample #7	Tantalum	0.3	9.8	Ta 100%	YES
Sample #15	Tantalum	0.4	13	Ta 100%	YES
Sample #13	T91 steel	0.4	6.1	Fe 89.35%, C 0.1%, Mn 0.45%, Si 0.35%, Cr 8.75%, Mo 1%	YES
Sample #10	T91 steel	0.6	9.1	Fe 89.35%, C 0.1%, Mn 0.45%, Si 0.35%, Cr 8.75%, Mo 1%	YES

In addition to the samples mentioned above, which were all irradiated in 2023, four more samples (*i.e.* flange bonded to foil) were produced, to be left unirradiated and used as reference for the post-irradiation examination, representing materials with pristine properties. Their foils, made of two materials (Steel T91 and pure Ta) in two different thicknesses (0.4 mm and 0.6 mm), are summarized in Table 3.

Table 3: Unirradiated assemblies – Foil mass and chemical composition

Sample number	Foil material	Foil thickness (mm)	Foil weight (g)	Foil chemical composition by weight	Irradiated samples
Sample #2	Tantalum	0.4	13	Ta 100%	NO
Sample #4	Tantalum	0.6	19.5	Ta 100%	NO
Sample #5	T91 steel	0.4	6.1	Fe 89.35%, C 0.1%, Mn 0.45%, Si 0.35%, Cr 8.75%, Mo 1%	NO
Sample #12	T91 steel	0.6	9.1	Fe 89.35%, C 0.1%, Mn 0.45%, Si 0.35%, Cr 8.75%, Mo 1%	NO

To create the beam window assembly, the foil and flange are brazed together. An example of the assembly drawing for one of the samples is presented in Annex A.6. The brazing process is carried out inside a vacuum oven (10^{-4} mbar). Prior to the process, brazing material (TiCuSil®) was

utilized in powder form between the window and flange at their contact surfaces (see Figure 3). The examples of the final brazed assemblies can be seen in Figure 4.

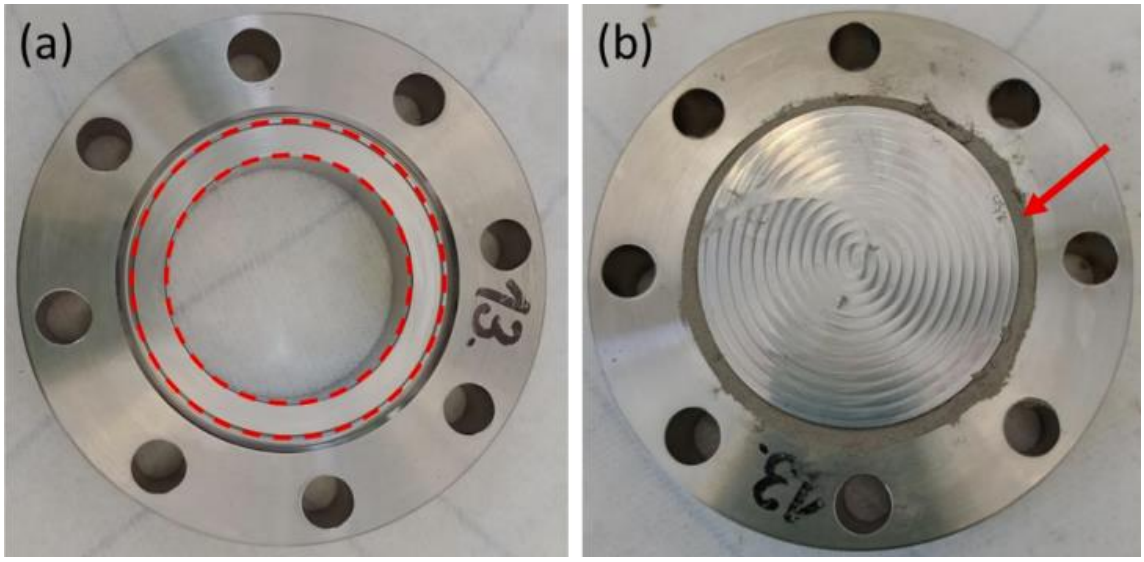

Figure 3: (a) Flange prior to the assembly (as machined). Region where brazing material was deposited is highlighted between dashed lines; (b) Flange and window after brazing material was deposited (still before brazing). Excess of brazing material flows to the neighbouring cavity (red arrow).

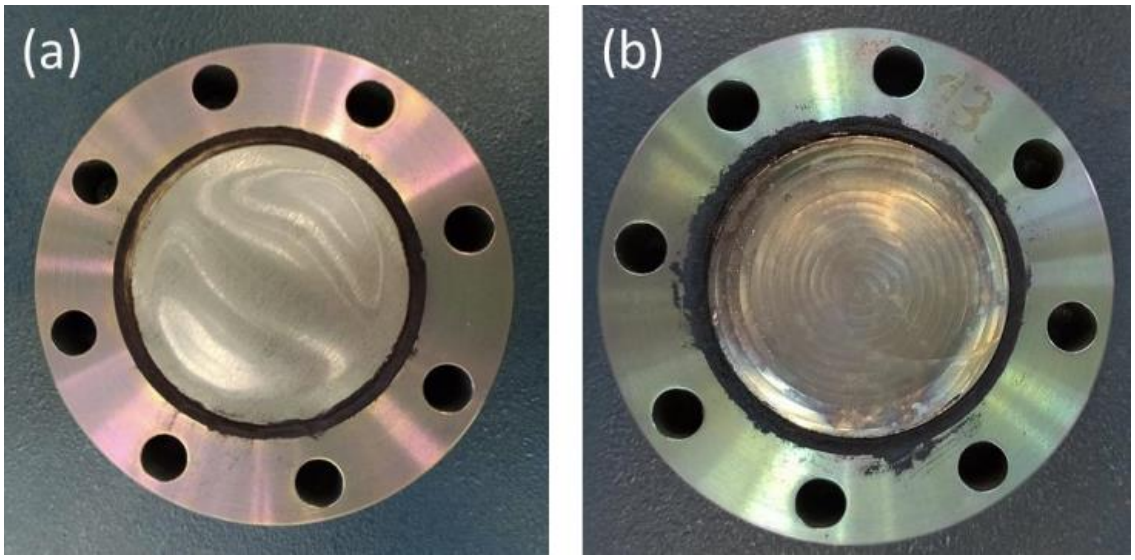

Figure 4: Examples of assemblies in the as-brazed conditions. (a) With Ta window, 0.4 mm; (b) with T91 window, 0.4 mm.

Different materials and thickness resulted in also different shapes (*i.e.* concave, convex) for the windows themselves after brazing. This can be attributed both to an accelerated creep at high temperatures, as well as to the differential thermal expansion coefficient between flange and window, especially when using tantalum discs (Figure 5).

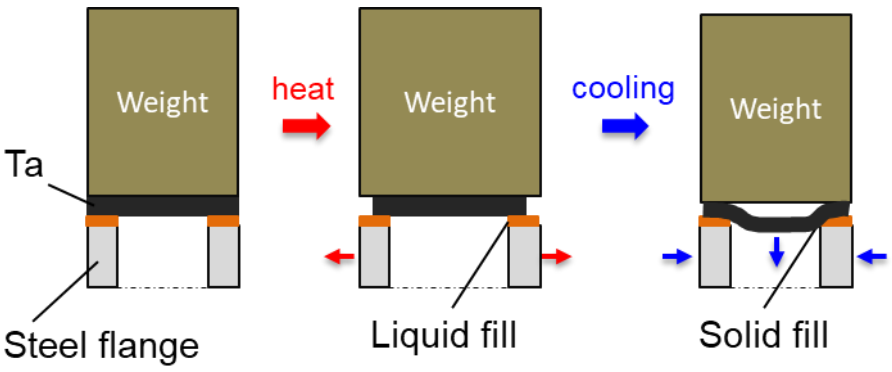

Figure 5 – Representation of the effects of differential thermal expansion between flange and window, a possible cause for modified window shape observed after brazing.

3 Irradiation configuration

The four assemblies described in Table 2 were irradiated in the IRRAD facility at CERN [4]. IRRAD is located on the T8 beam-line at the CERN PS East Hall (building 157) where the primary proton beam with a momentum of 24GeV/c is extracted from the PS ring. As shown in the figure below, the space allocated for irradiation tests in the East Hall is shared between two irradiation facilities: the IRRAD proton facility is located upstream while the CHARM mixed-field facility is implemented downstream. Since most of the protons pass through the IRRAD facility without interacting, the mixed-field facility can profit from the same protons used by IRRAD. Inside CHARM, these protons impinge on a target surrounded by a well calculated shielding configuration. The IRRAD proton irradiation facility at the PS East Area is maintained and operated by the irradiation team within the EP-DT-DD section at CERN.

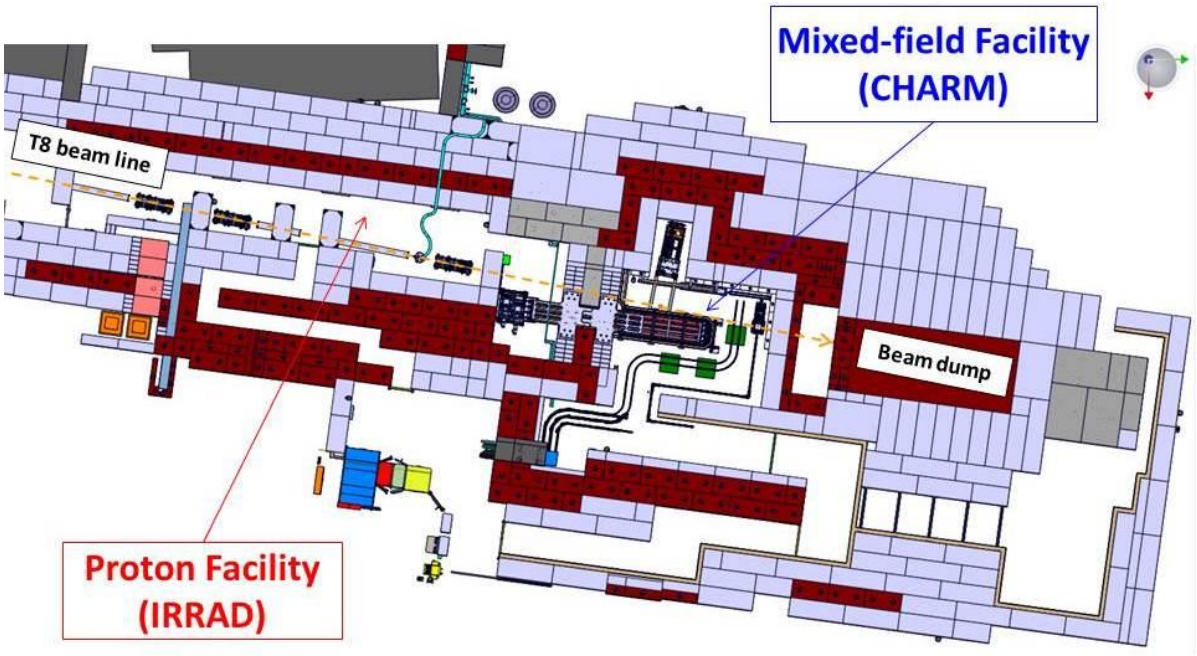

Figure 6: Location of the IRRAD proton area within the EA-IRRAD Facility in the CERN East Hall (building 157).

The IRRAD facility is subdivided in three zones (going from upstream to downstream) according to the nature of the samples to be irradiated. In between each irradiation zone, a separation wall 80cm-thick (with a hole to allow the beam to pass through) is placed in order to reduce the radiation background during irradiation and to minimize the ambient equivalent dose to the personnel during the access to the area. As visible in the picture below, in order to reduce further the secondary radiation produced by the interaction of the proton beam with the air, section of vacuum beam-pipes are installed in the empty space between the installed irradiation systems.

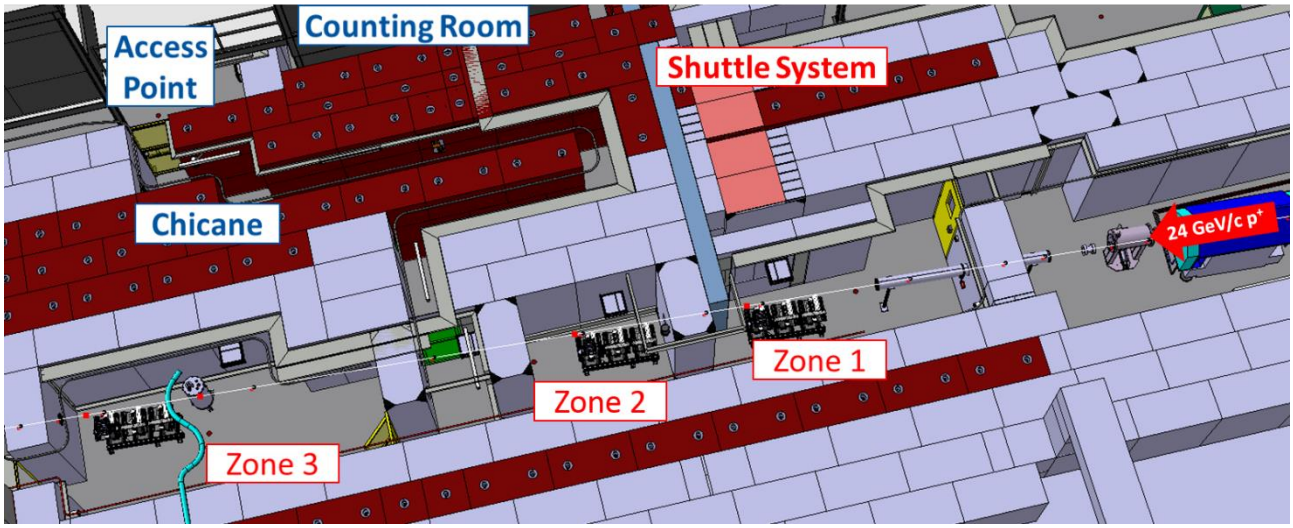

Figure 7: Detailed Layout of the IRRAD Proton Facility.

The four samples in the scope of this deliverable were positioned in series in a sample holder, as shown in

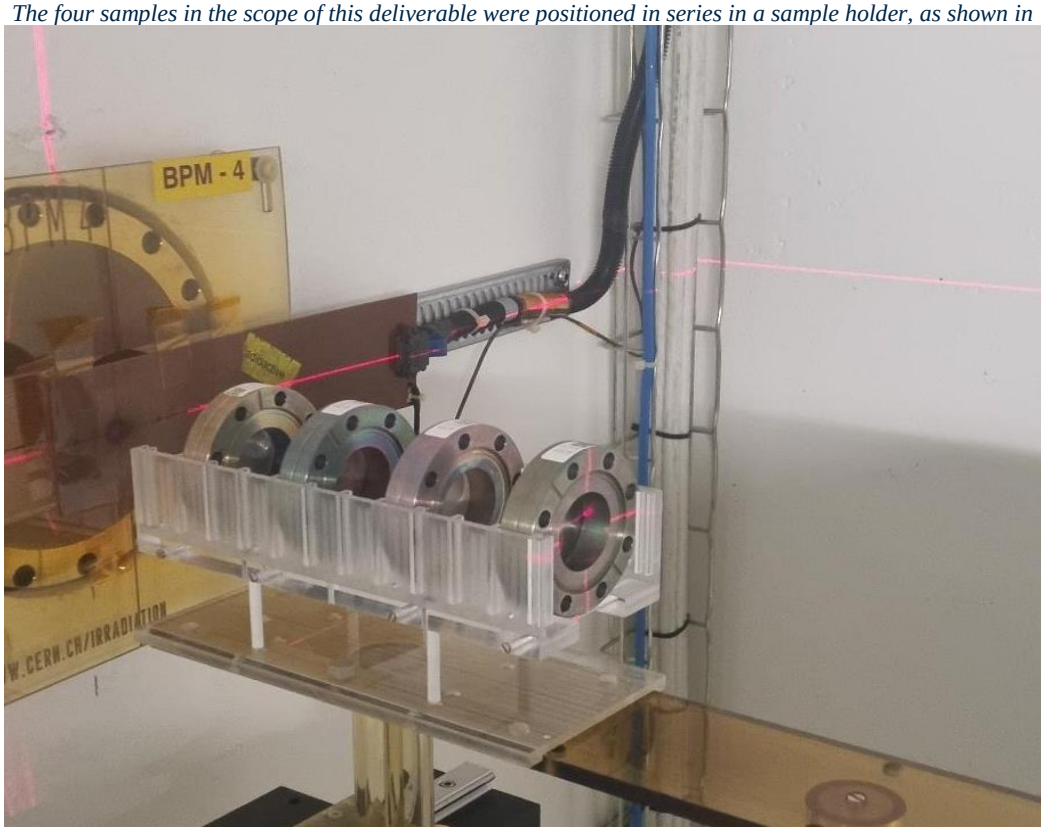

Figure 8.

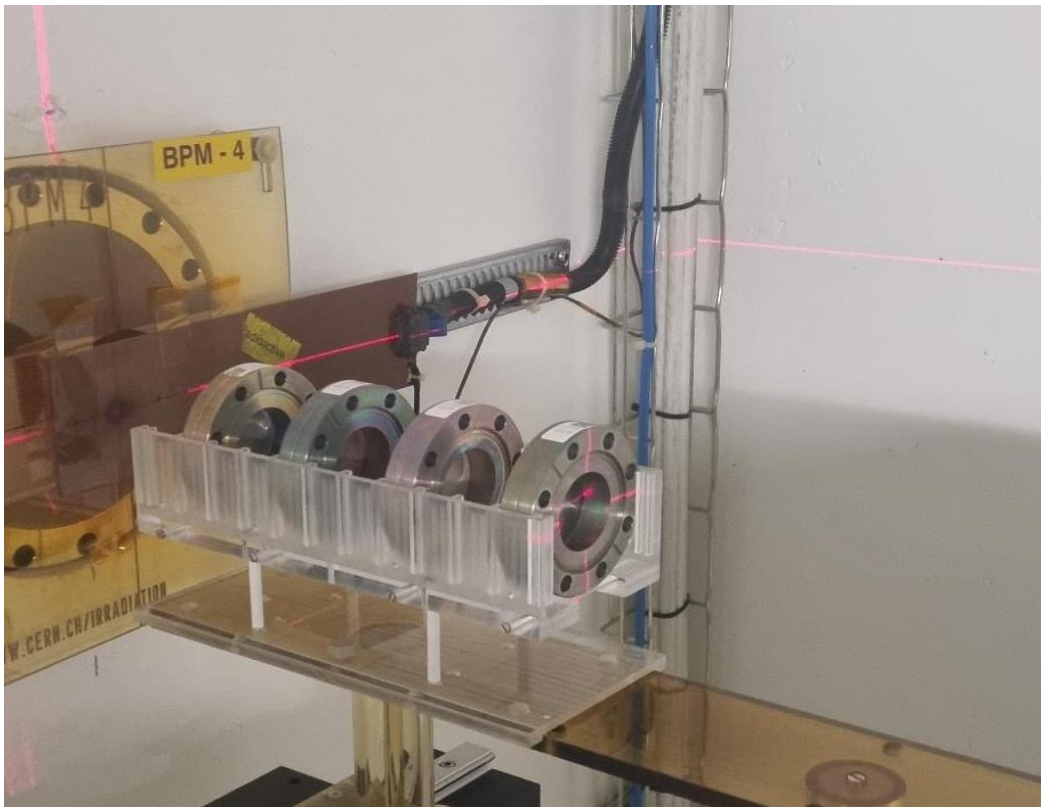

Figure 8: Sample holder with IFAST beam windows assemblies at IRRAD.

3.1 IRRADIATION PARAMETERS: DOSE AND FLUENCE

The irradiation was performed in the period 6th September – 11th October, with the IRRAD protons beam (25 GeV/c). The irradiation parameters are summarized in

Table 4.

Table 4: Dose and fluence on the IFAST D4.3 sample holder, during 2023 IRRAD campaign.

Sample number	**Foil material**	**Foil thickness (mm)**	**Order in the stack (1: upstream, 4: downstream)**	**Average fluence (protons/cm²)**		**Average dose (MGy)**	
				Circular area ø20mm	***Circular area ø10mm***	***Circular area ø20mm***	***Circular area ø10mm***
Sample #7	Tantalum	0.3	1	1.07e16	1.96e16	1.97e6	3.61e6
Sample #15	Tantalum	0.4	4	1.07e16	1.96e16	1.97e6	3.61e6

Sample #13	T91 steel	0.4	3	1.07e16	1.96e16	2.49e6	4.56e6
Sample #10	T91 steel	0.6	2	1.07e16	1.96e16	2.49e6	4.56e6

The fluence on target was measured online with the IRRAD beam monitors. Knowing this, the dose on target can be calculated, with the formula [7]:

$$Dose\ [Gy]\ =\ 1.602 \cdot 10^{-10} \cdot (dE/dx)_{min} \cdot \Phi_p$$

Where: Φ_p is the proton fluence in cm^{-2}, and $(dE/dx)_{min}$ is the minimum stopping power in MeV·cm^2/g, that depends on the material impacted by the beam. The value of this constant is 1.146 MeV·cm^2/g for tantalum and 1.451 MeV·cm^2/g for T91 [8].

Since the proton beam transverse cross-section follows a gaussian distribution (see section 3.2 for more on this), two values of fluence and of dose are provided, averaged over the circular irradiated area, assuming, respectively, 20 and 10 mm diameter for the averaging.

3.2 Irradiation parameters: Displacements-Per-Atom (DPA) and gas production

To characterize radiation-induced structural damage in the irradiated beam windows, two quantities have been assessed:

- Displacements per atom (DPA): the number of atoms displaced from their original lattice position.
- Production of residual H and He nuclei that are stopped in the sample, forming “bubbles”, which may in turn lead to swelling and cracks. This effect is quantified as the ratio of gas atoms to the original number of atoms of the sample, expressed in atomic parts per million (appm).

Because a direct measurement of either gas production or DPA is not readily feasible, Monte Carlo (MC) simulations have been performed instead, employing the general-purpose code FLUKA [9][10][11]. The simplified geometry, displayed in Figure 9, has been adopted, including the foils themselves, the steel flanges, and the air surrounding the system. Simulations assumed a 24 GeV/c proton beam with a Gaussian momentum spread of 0.1 GeV/c, centred on the targets and with no angular divergence, and a Gaussian transverse profile with 1.2 cm FWHM. The sequence of targets considered along the beamline is detailed in Figure 9. The first and last target with respect to the beam direction (targets 7 and 15) are made of Ta, while the two middle targets (10 and 13) are made of T91 steel.

FLUKA simulations reported here accounted for the transport and interaction of leptons, hadrons (including ions), and photons. The FLUKA “DAMAGE” defaults were selected, adapted to radiation-damage calculations, overriding transport and production thresholds of electrons/positrons to 100 keV and of photons to 10 keV. To attain statistically significant results, $1.6 \cdot 10^9$ primary

protons were considered, which was sufficient to attain a statistical uncertainty of approximately 5% on the DPA and gas production results. The estimated physical quantities, extracted from the MC simulation on a per-primary basis, have been scaled here to the experimentally measured integrated fluence on the entire beam window (for the aforementioned beam profile), extracted from the measured fluences on two foils during the irradiation campaign.

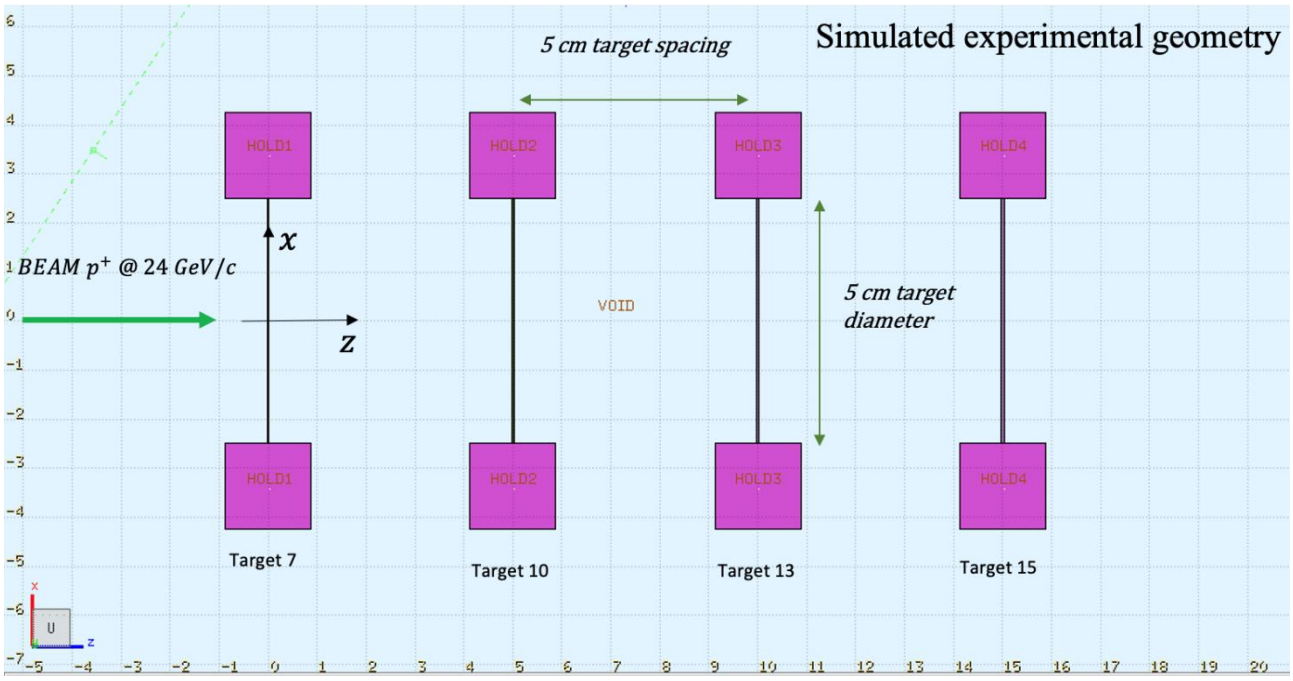

Figure 9: FLUKA simulation geometry. Lengths are in centimetres.

3.2.1 DPA

DPA has been estimated in FLUKA relying on the athermal-recombination corrected DPA (arc-DPA), a recent prescription introduced by Nordlund *et al. [12]*, in which the number of sustained ion-hole pairs N_d is given by

$$N_d(T_d) = \begin{bmatrix} 0\,, & T_d < E_d \\ 1\,, & E_d < T_d < \dfrac{2E_d}{0.8} \\ \dfrac{0.8T_d}{2E_d}\,\xi_{\mathrm{arcdpa}}(T_d), & T_d > \dfrac{2E_d}{0.8} \end{bmatrix},$$

where T_d is the available energy for creating atomic displacements, E_d is the damage threshold, and ξ_{arcdpa} is given by:

$$\xi_{\mathrm{arcdpa}}(T_d) = \frac{1 - c_{\mathrm{arcdpa}}}{\left(\frac{2E_d}{0.8}\right)^{b_{\mathrm{arcdpa}}}}\, T_d^{b_{\mathrm{arcdpa}}} + c_{\mathrm{arcdpa}}\,.$$

The arc-DPA evaluation therefore relies on three material-dependent parameters: E_d, b_{arcdpa}, and c_{arcdpa}, available in the literature only for elementary pure materials. For the present simulations, arc-DPA parameter values were extracted from the compilation by Konobeyev *et al.* [13], reported in Table 5: arc-DPA parameters used for the simulation, including their significant systematic uncertainties of the order of 20%-30%.

Table 5: arc-DPA parameters used for the simulation

Parameter	**Ta**	**T91 Steel (main components)**		
		Iron	Chromium	Molybdenum
E_d (eV)	90 ± 18	40 ± 8	40 ± 8	65 ± 13
c_{arcdpa}	0.72 ± 0.2	0.286 ± 0.09	0.37 ± 0.10	0.46 ± 0.13
b_{arcdpa}	-0.5	-0.568	-1.0	-1.0

For T91 steel, the arc-DPA parameters were specified for the most abundant chemical elements in its composition. It should be noted that the displacement and recombination of atoms in a material depends on the molecular and crystal structure of the material. However, due to the lack of explicit arc-DPA parameters for the T91 steel (a compound material), a mass-ratio weighted sum of the arc-DPA for each of its constituent parameters was considered.

The DPA was scored on a series of cylindrical meshes, exactly overlapping the beam windows, with a spatial resolution of ~0.1 mm resolution in the radial coordinate on the plane transversal to the beam (with 50 angular bins), and ~0.01 mm resolution along the beam in the depth of the thin foils. The resulting DPA estimates are shown in Figure 10 and Figure 11. Figure 10 displays the dependence of the DPA on the radial distance in all foils; unsurprisingly the DPA follows the same shape of the Gaussian beam profile, and the Ta samples exhibit a higher DPA than the T91 samples.

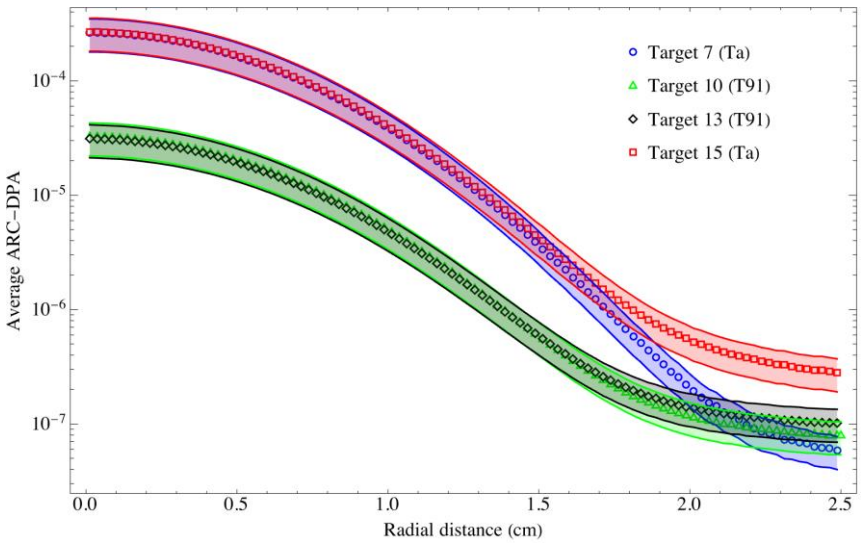

Figure 10: Average arc-DPA as a function of radial distance. The coloured bands around the points represent an estimate of the systematic uncertainties.

Figure 11 displays the highest level of DPA across slices perpendicular to the beam, as a function of depth in each sample. The Ta samples undergo higher DPA levels, of the order of $3 \cdot 10^{-4}$ DPA, whereas those of T91 are lower, of the order of $3 \cdot 10^{-5}$ DPA. The longitudinal variation, on the order of 10-20% across the sample, closely follows the energy deposition profile.

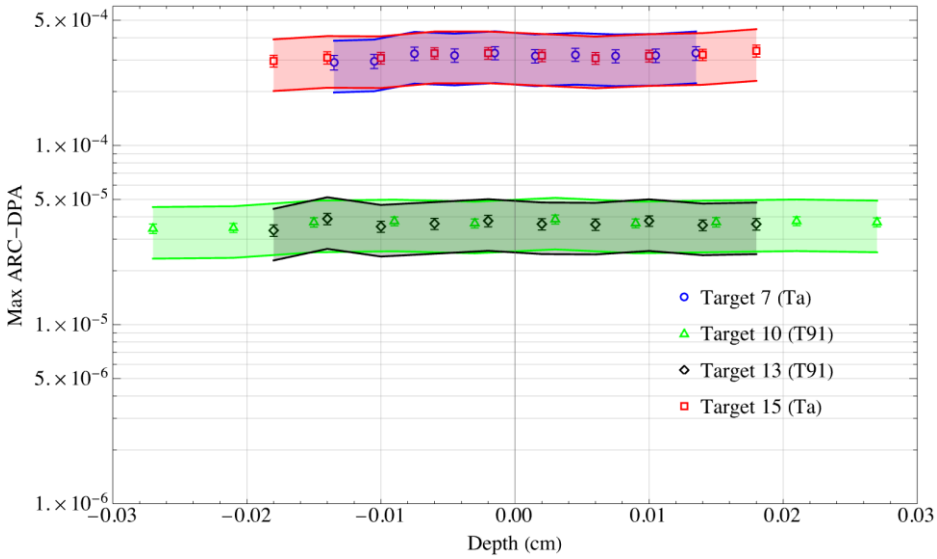

Figure 11: Maximum arc-DPA along transverse slices of the beam samples, as a function of depth in each sample. The points carry statistical error bars and the coloured bands around the points represent an estimate of the systematic uncertainties due to the uncertainty in arc-DPA parameters.

3.2.2 Gas production

The number of H and He nuclei produced due to beam interactions and stopped within the beam windows was also scored. Results of this analysis are shown in Figure 12. Gas production is more severe in Ta targets than the T91 ones, for both H and He, with 0.01 – 0.02 appm in the former and 0.003-0.005 appm in the latter. The observed longitudinal profile is as expected for a high-energy

beam of protons incident on a thin target, with a decrease in stopped gas atoms near the entrance and exit surfaces.

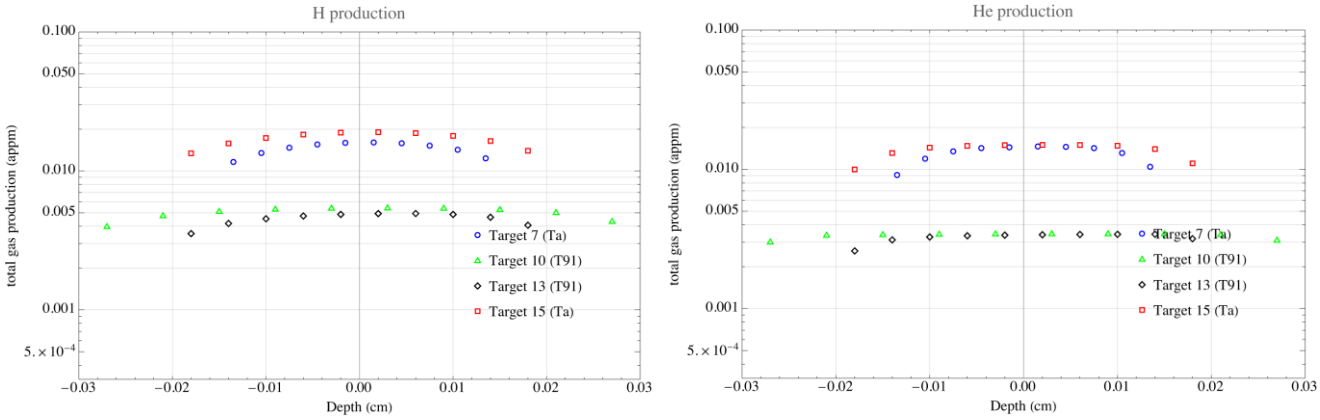

Figure 12: Gas production, H and He respectively, in the beam windows

4 Characterization of unirradiated and irradiated samples

As explained, two identical sets of beam windows have been prepared: the first one was irradiated, and the second remained unirradiated. The second set of assemblies represented thus the reference of pristine sample to be compared with the irradiated ones. The characterization of the two sets was performed in April and May 2024, after about 6 months of cooldown, which led to the residual samples activation shown in Figure 13.

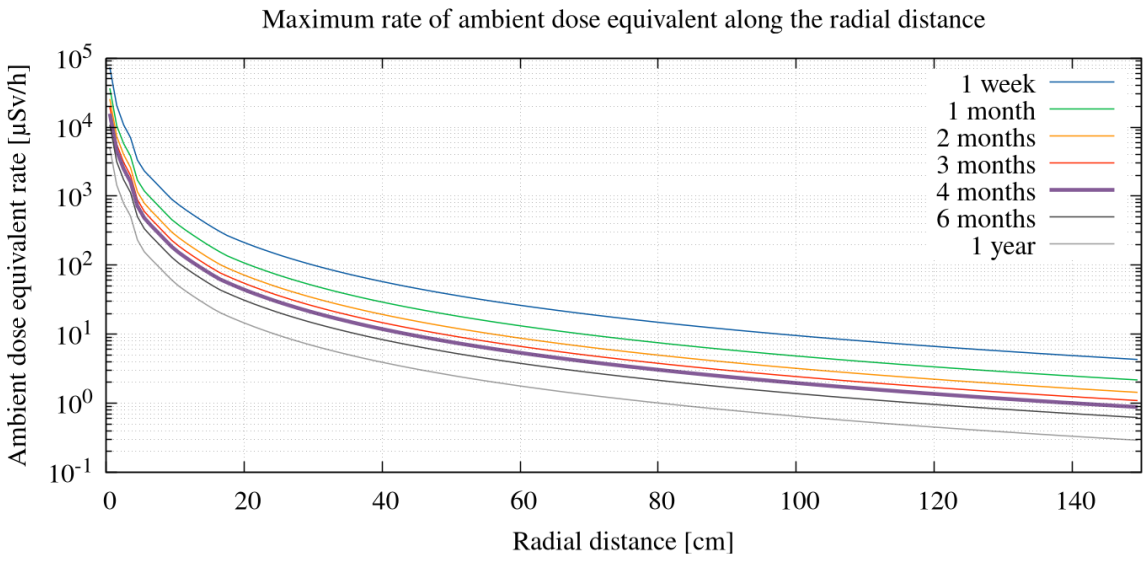

Figure 13: Radial projection of the ambient dose equivalent rate from the complete set of irradiated samples, for different cooling times.

The full list of the tests performed is reported in Table 6. On of the most important measurements concerned the thermal conductivity: in fact, this is the property controlling the whole thermal and

thermomechanical response of the beam window to the passage of the beam. A high thermal conductivity ensures evacuation of the beam heating both in steady-state and in pulsed applications, consequently also minimizing the thermal stresses and strains generated by the beam interaction. This property depends on the material microstructure, which is affected and damaged under beam irradiation. The possible change of this property after beam irradiation needs to be measured and quantified. For the same reason, several metallographic inspections, aiming at inspecting the microstructure in detail, were also performed (computed micro-tomography, optical and scanning electron microscopies).

Table 6: arc-DPA parameters used for the simulation

Test	**Testing time**
Dye penetrant	10 min per specimen
Computed tomography	1 day per specimen
Optical microscopy	30 min per specimen
SEM	2-4 h per specimen
Electrical conductivity	1 min per specimen
Thermal conductivity	Derived from electrical conductivity

The following sub-sections report the main results of each test.

4.1 DYE PENETRANT TEST

This test was performed at RHP's premises on all of the eight samples, after production and after brazing the foil with the stainless steel flange. Its objective was to evaluate the leak tightness of the brazing. Infiltration tests were performed using the dye penetrant method, whereby the dye and developer fluids were sprayed in opposite sides of the beam window, according to the example provided in Figure 14. The pink dye remained on the bottom of the assembly for 24 hours, before the developer fluid could be applied at the opposite side. The test was reproduced on every manufactured assembly.

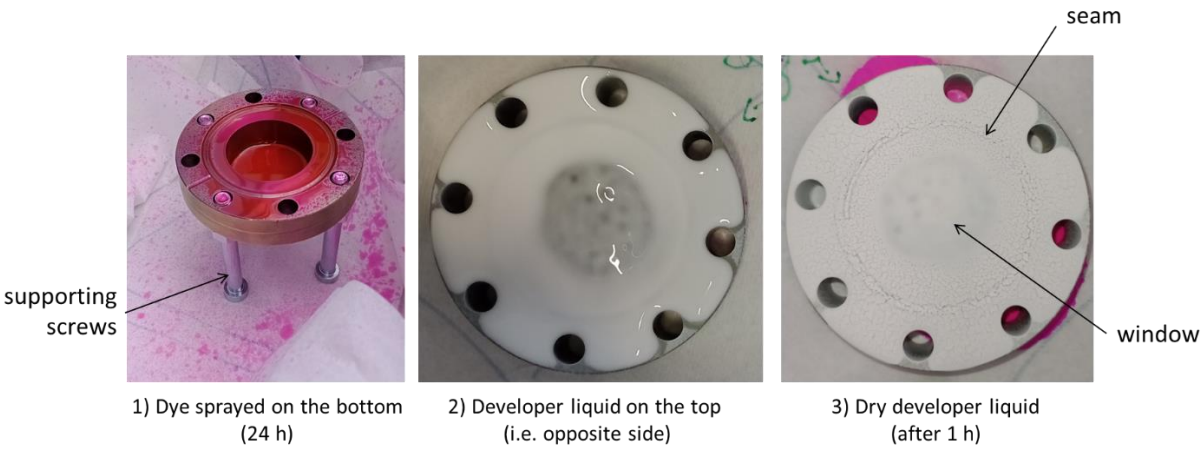

Figure 14 – Stages of infiltration test

A sample was considered as having failed the test if the pink color was detected anywhere around the seam region. Occasional leakage of the pink dye liquid at and/or surrounding the screw holes were dismissed. Examples of test results can be seen in Figure 15. A summary of the test results is available in Table 7.

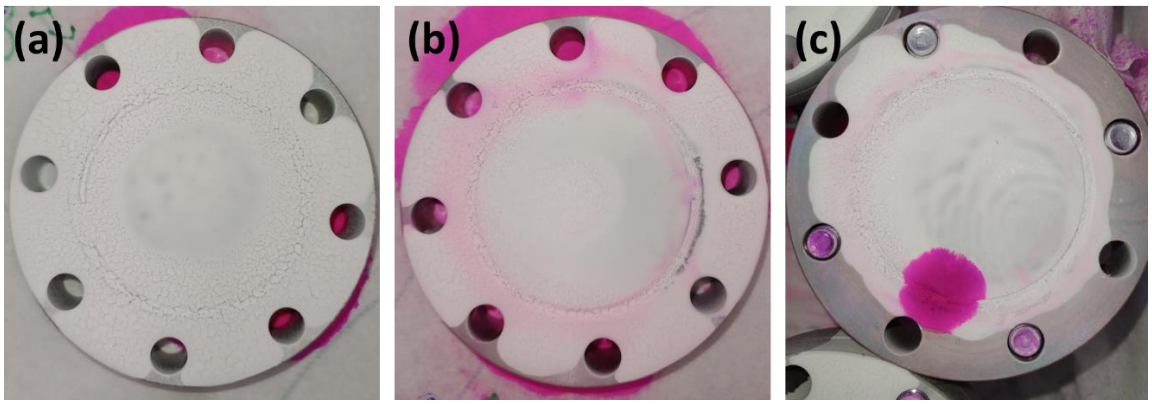

Figure 15 – Possible results of the infiltration tests. (a) No pink marks found around the seam region (OK); (b) pinkish coloration around the seam region (Fail); (c) severe localized leakage detected at the seam region (Fail).

Table 7: Summary of infiltration test results.

Flange ID	Window material	Window thickness [mm]	Window shape	Penetration test
7	Ta	0.3	Convex	OK
10	Ta	0.4	Concave	Leak
13	T91	0.4	Concave	OK
15	T91	0.6	Convex	OK
2	Ta	0.4	Concave	OK
4	Ta	0.6	Convex	Leak

5	T91	0.4	Convex	Leak
12	T91	0.6	Convex	OK

As explained in section 2, after brazing, due to the accelerated creep at high temperatures, as well as to the differential thermal expansion coefficient between flange and window, the windows all presented a certain degree of curvature, taking convex or concave shapes. For the same reason, due to the high stresses at the foil/flange interface, 3 assemblies out of 10 presented micro-leaks highlighted by the dye penetrant testing.

This test shows that the procedure of brazing needs further optimization, and this will be in the scope of the remaining work in WP4.3 before the end of the project. However, even if not all assemblies are UHV-tight, the mechanical adherence between foils and windows is macroscopically good, and the leaks come from micro-porosities. As part of the scope of the irradiation campaign was to assess macroscopically the mechanical resistance of the foil/flange interface, we judged that the presence of micro-porosities in assembly #10 was not precluding its inclusion in the sample holder to be irradiated in IRRAD.

4.2 COMPUTED MICRO-TOMOGRAPHY

Computer tomography (CT) allows to obtain a 3D scan of the examined component. X-rays produced by a source in the form of a cone beam pass through the sample and are partially absorbed, partially reflected by a detector that captures the beam and creates a 2D X-ray image. Thanks to the 360-degree rotation of the sample, approximately 2,000 X-ray images can be captured, and used to reconstruct the 3D volume. The resolution of a 3D CT image strongly depends on two factors: the dimensions of the sample (Region of Interest of the scanned sample) and the spot size, which is influenced by the scanning power (the higher the power, the larger the spot and the worse the resolution). All beam windows were scanned with a voxel (3D pixel) size of 35 µm, which was the maximum possible level of refinement given the size of the samples. Images and video-scans were captured for each sample.

In the images of non-irradiated samples, some defects were identified on all samples, which are most likely the result of the brazing filling spilling onto the foil, creating voids in the brazing filling. After verifying the thickness of the foil for samples #5 and #12 (0.4 mm and 0.6 mm, see Figure 16 and Figure 17), it is clearly visible that these defects occur in the brazing filler.

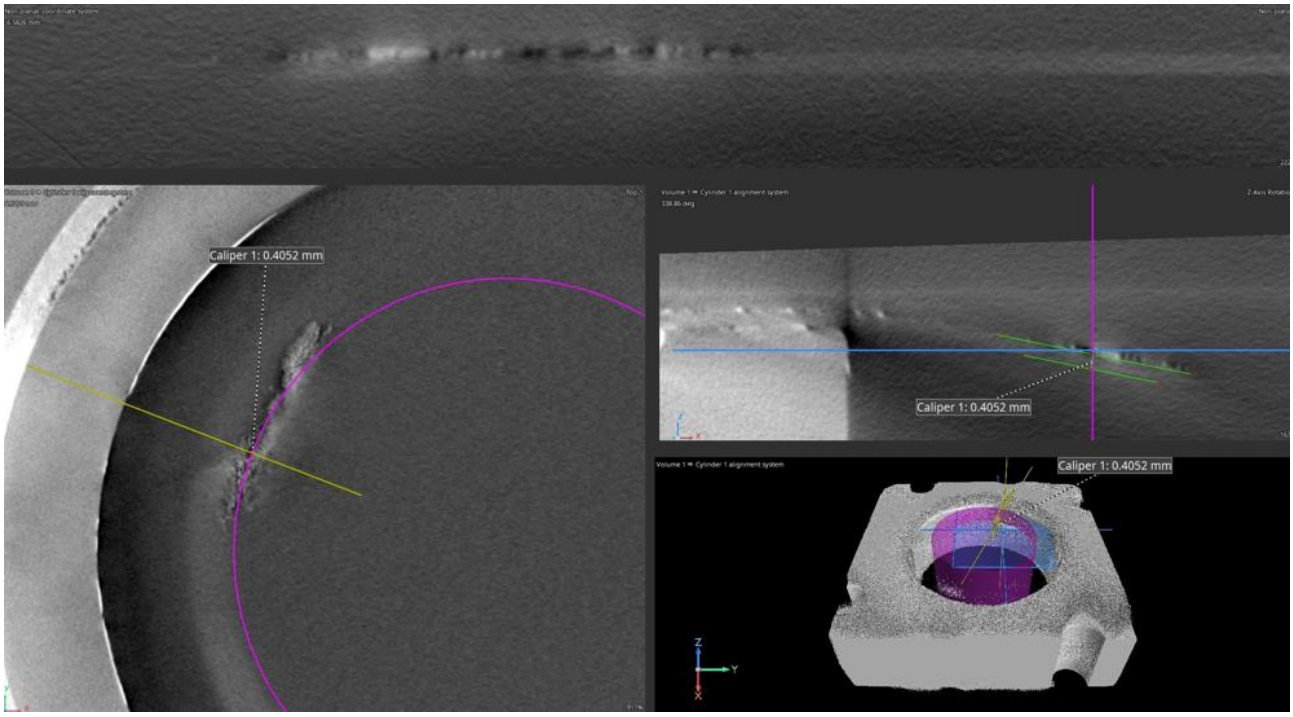

Figure 16: Sample #5 (T91), CT scan.

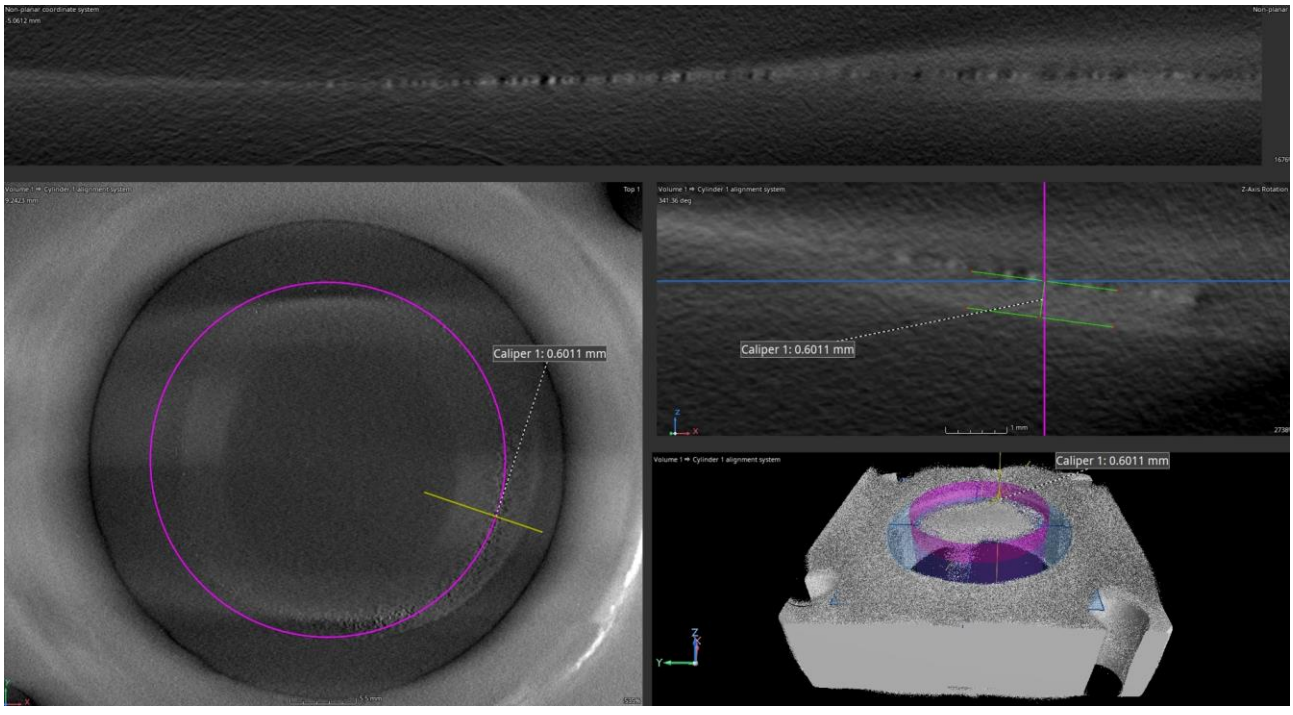

Figure 17: Sample #12 (T91), CT scan.

No defects were visible in the Tantalum samples (#2 and #4), see Figure 18 and Figure 19. However, this might also be due to the worse contrast available when analysing this material. This will be better scrutinized with the microscopy measurements, that can go to a much higher level of detail (section 4.3).

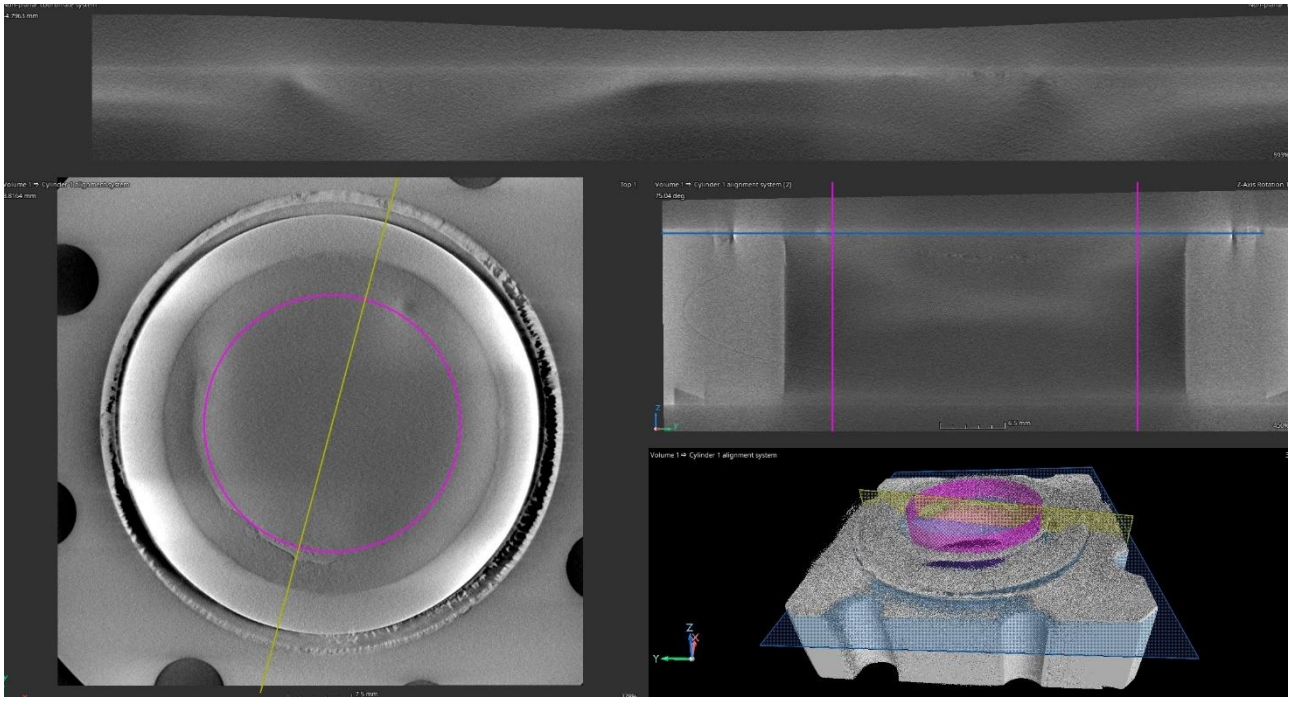

Figure 18: Sample #2 (Ta), CT scan.

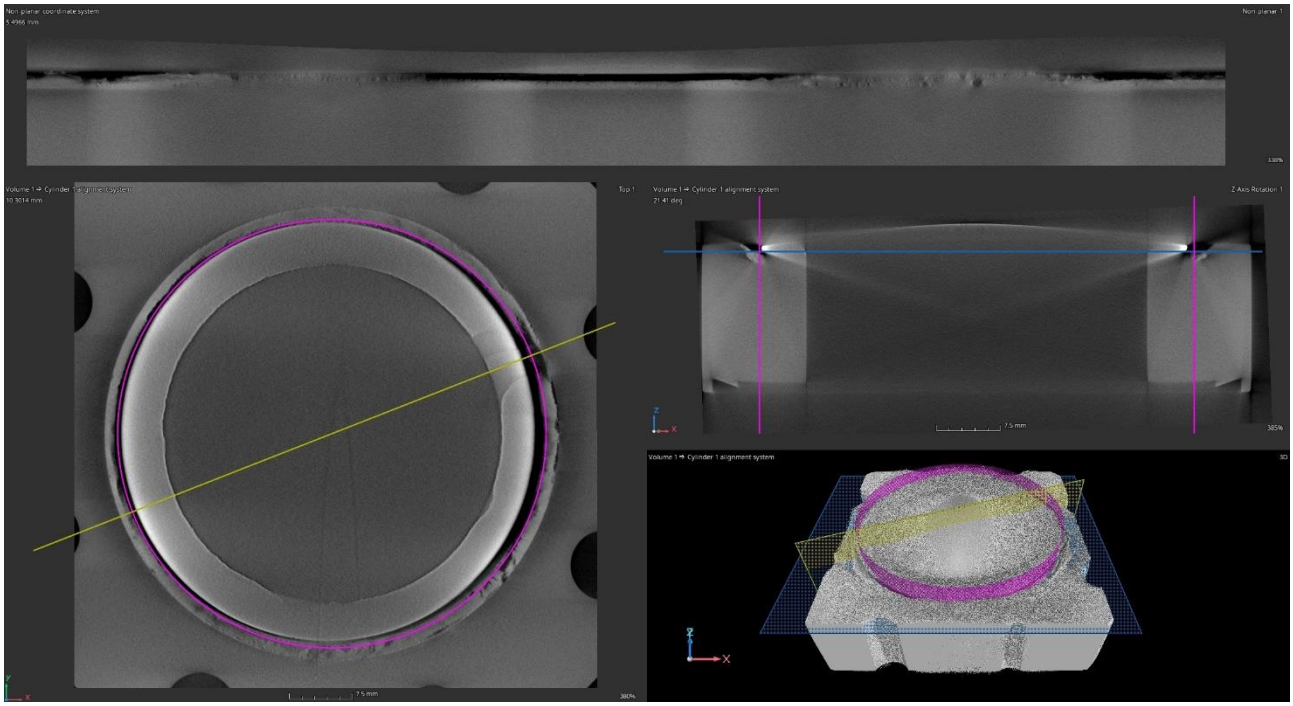

Figure 19: Sample #4 (Ta), CT scan.

In the irradiated T91 samples, apart from the traces coming from the vacuum brazing that were already visible in the unirradiated samples, no defect is observable in the innermost circular area exposed to the proton beam (Figure 20 and Figure 21).

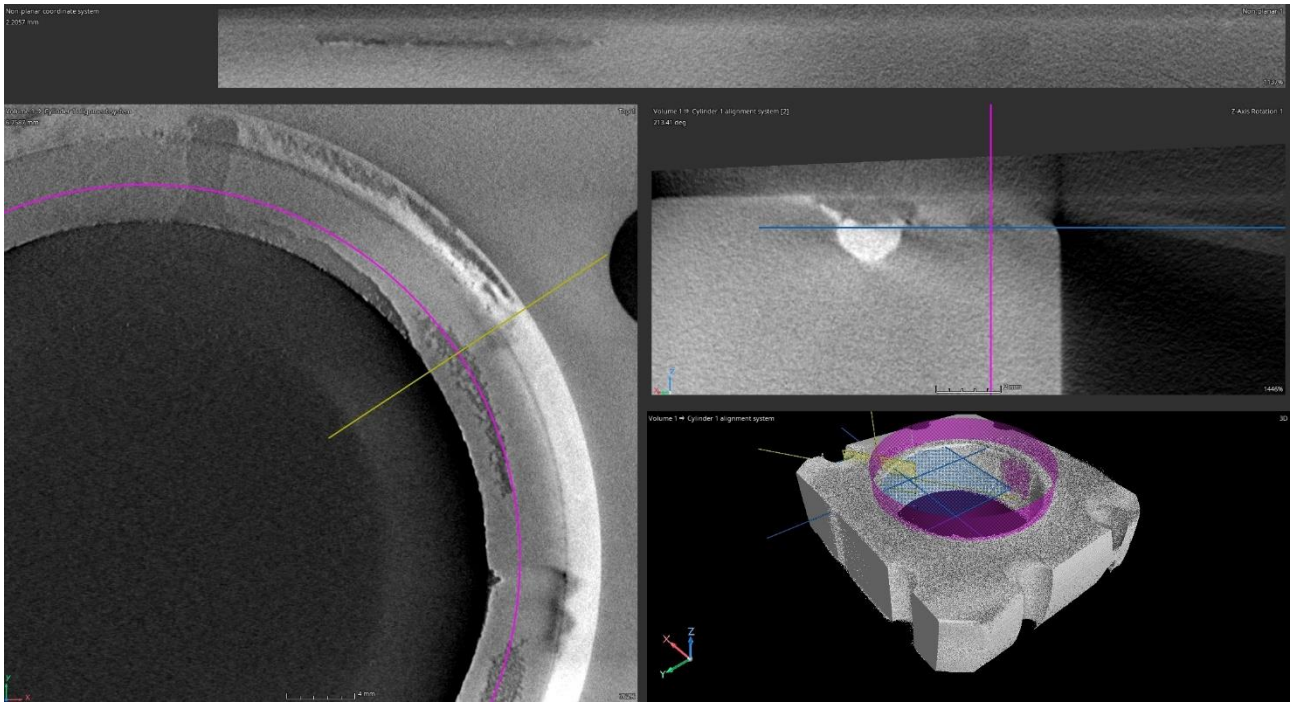

Figure 20: Sample #10 (T91), CT scan. Some peripheric inclusions due to the foil/flange brazing is visible, but nothing is present in the beam region.

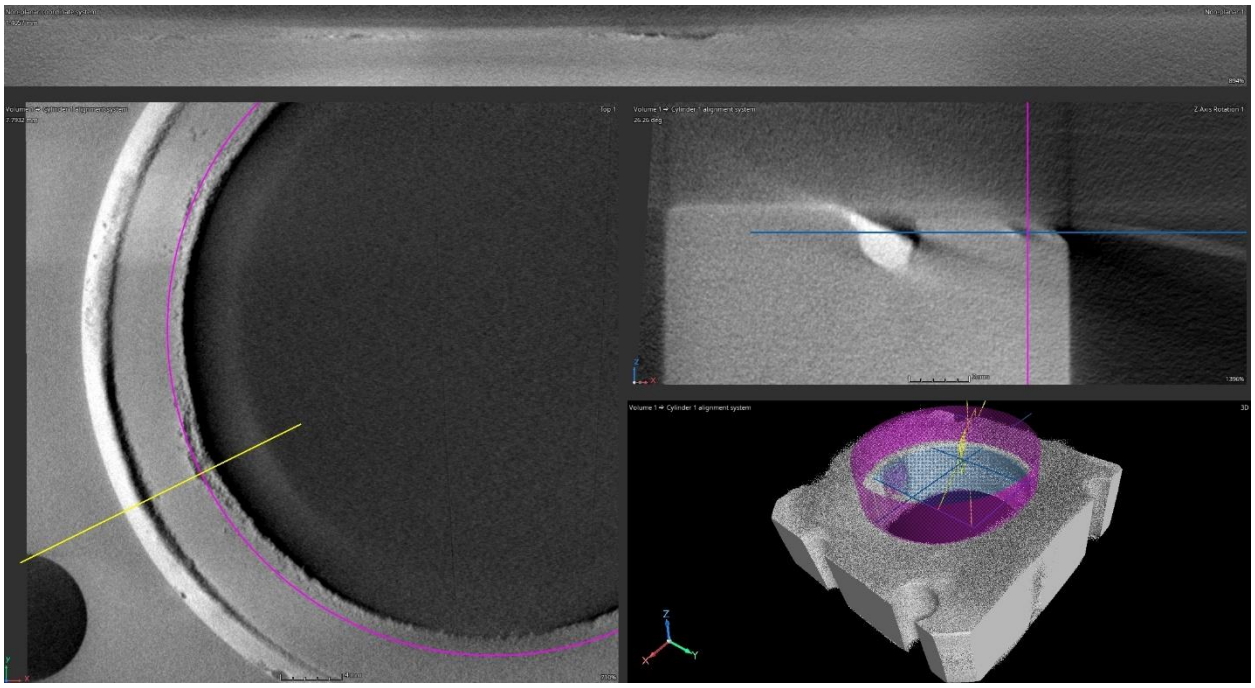

Figure 21: Sample #13 (T91), CT scan. Qualitatively similar to sample #10.

In tantalum irradiated samples, traces in the central region irradiated with protons are visible (Figure 22 and Figure 23), potentially hinting some modification in the material microstructure.

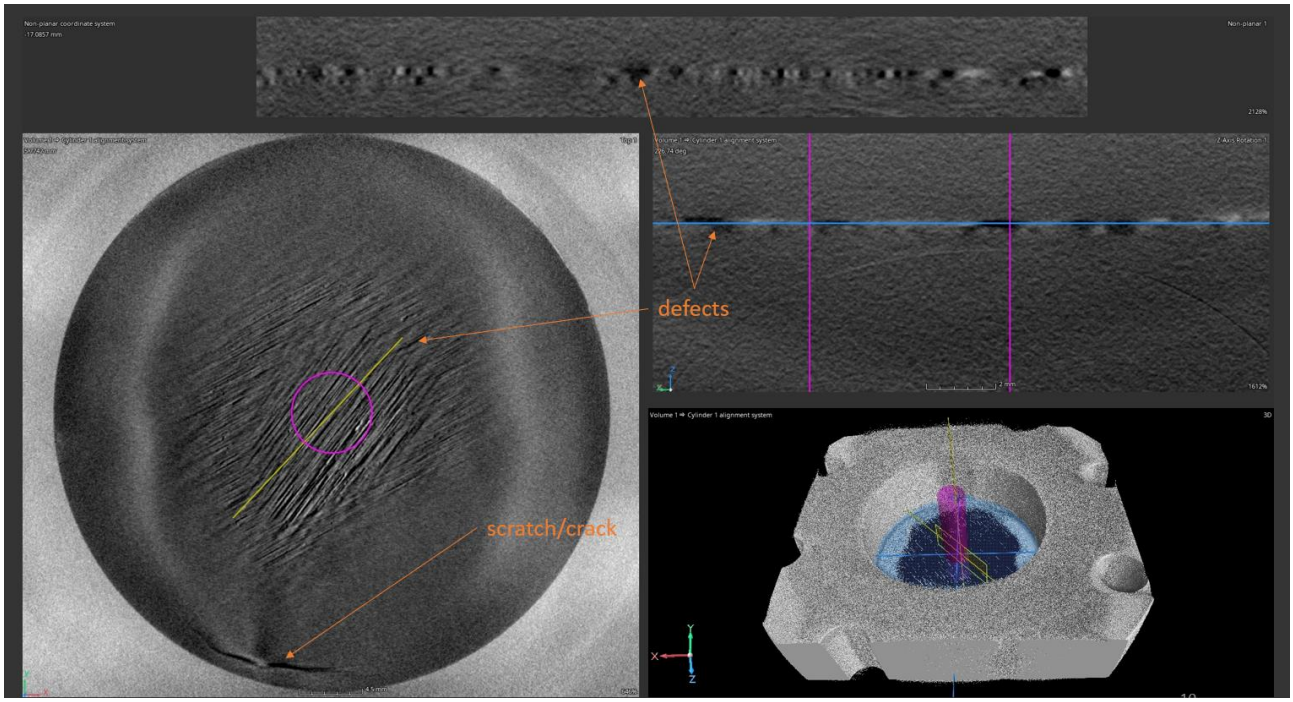

Figure 22: Sample #7 (Ta), CT scan.

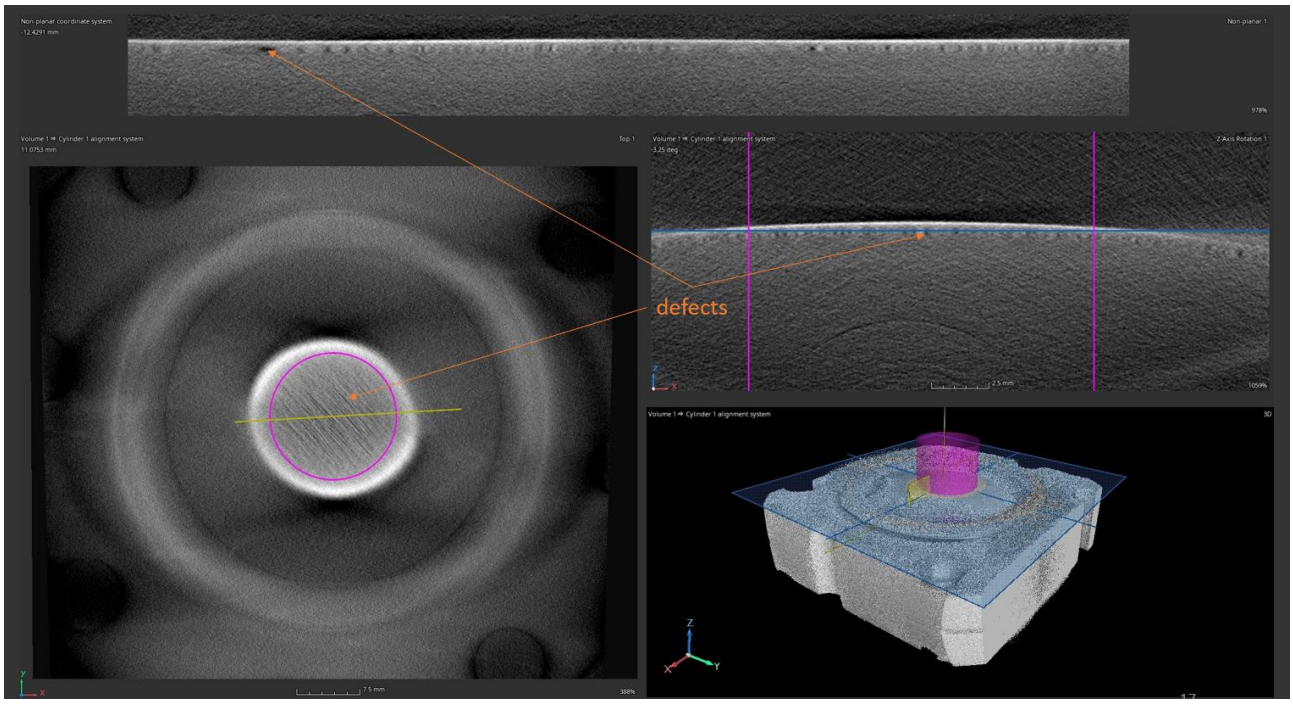

Figure 23: Sample #15 (Ta), CT scan.

As a conclusion of the computed micro-tomography, the analyses showed defects due to the brazing that were already highlighted by the dye penetrant tests. After irradiation, no macroscopic defect

was highlighted in any of the targets; however, the tantalum samples showed a pattern in the microstructure, in the region irradiated by the beam, that could be compatible with a radiation-induced effect. This will be better observed with the more refined microscopies described in the following sub-section.

4.3 OPTICAL MICROSCOPY AND SEM

Microscopic observation was performed of both reference (ref.) and post-irradiated samples. The flange, the metallic foil, and a brazing material (black region) are distinguishable on the OM images (see

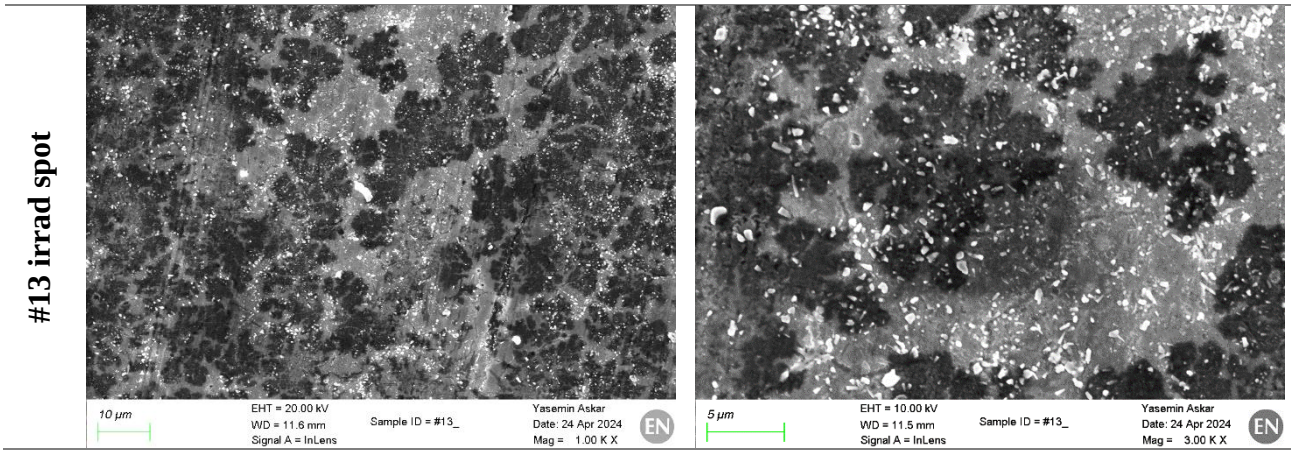

Figure 24).

In general, all samples when observed by OM and SEM show a rough surface with visible machining marks. Additionally, the black powder of the brazing material (Ti rich) is spread and can be found in different locations around all the samples (reference and irradiated) as shown in Figure 25.

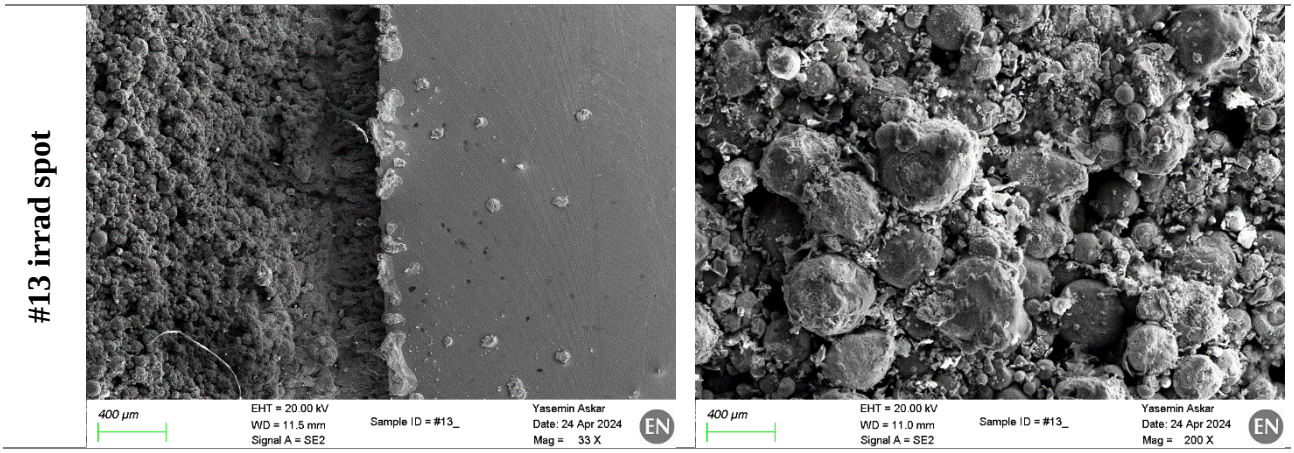

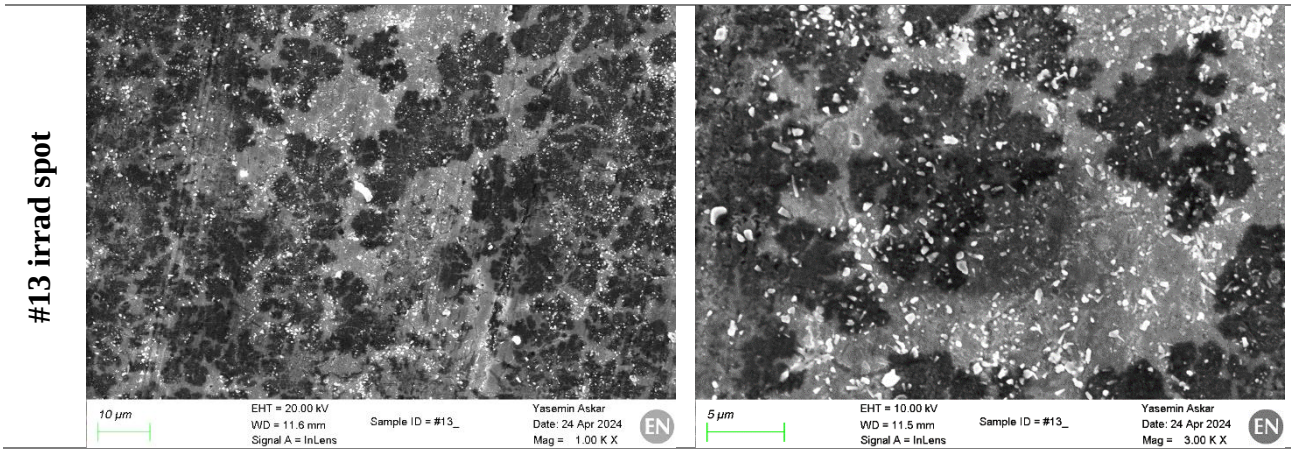

Figure 24: Sample #13 (T91), different levels of magnification.

At the irradiated areas on T91 samples (Sample_#10 and #13 -

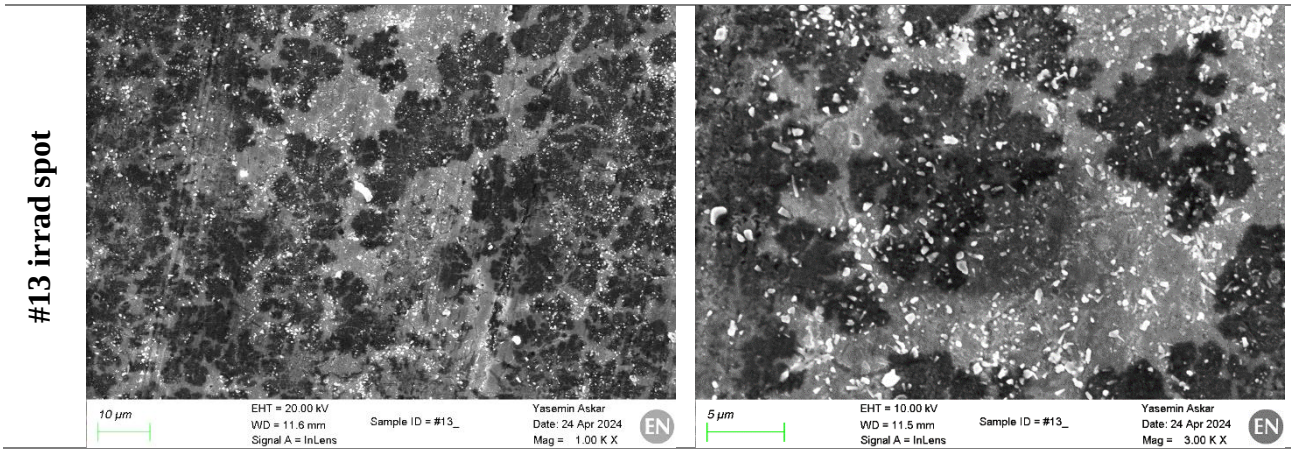

Figure 24) superficial features are visible with relative chemical contrast (similar but not coincident with the grain structure) as shown in the image. They are mainly superficial and based in atomic number contrast indicating some local contamination/oxidation (Figure 2, SOI_1-AsB).

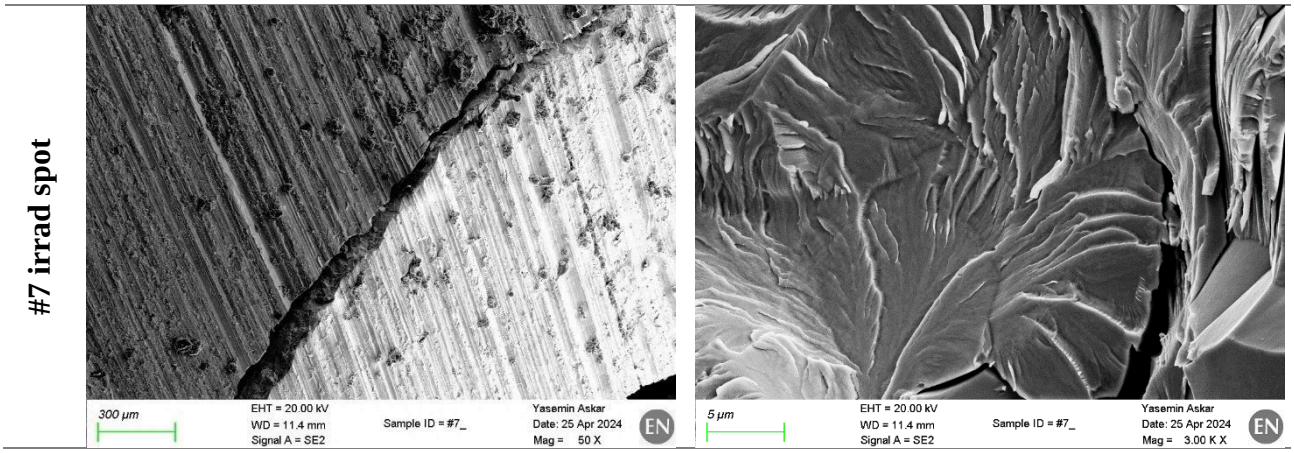

Figure 25: Sample #7 (Ta), different levels of magnification.

Sample #7 (Ta) presents a fracture corresponding with one of the flange edges. The crack displayed a brittle aspect, most probably induced by the mechanical load during manipulation.

Additionally, the grain boundaries appear more defined on the irradiated locations than in non-affected areas, as shown in Figure 26.

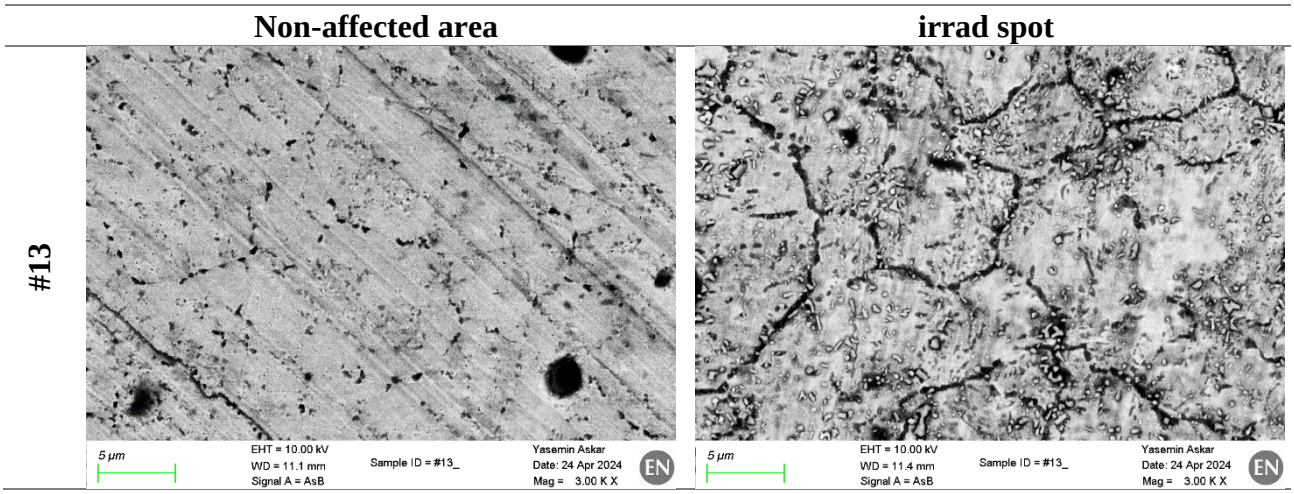

Figure 26: Sample #13 (T91), non-irradiated and irradiated region comparison.

EDS analysis confirmed the expected elements for the metallic foils and the brazing filler Ticusil® and no major differences were found between the irradiated and non-irradiated areas in terms of oxidation. Worth to mention that traces of other elements were also detected on the surface of the samples like C, Na, Mg, Si, Ca, V, Cl, S, Cu in varying amounts depending on the sample and the part observed.

	OM	SEM detector: SE2 / Inlens /AsB	
Ref_#4 (Ta)	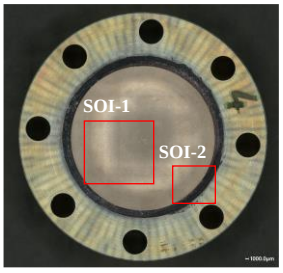	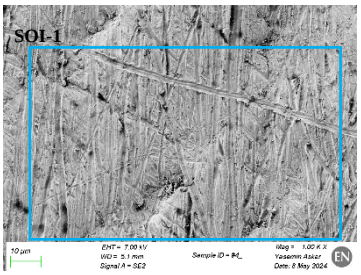	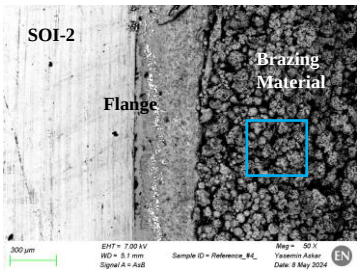
Ref_#5 (T91 steel)		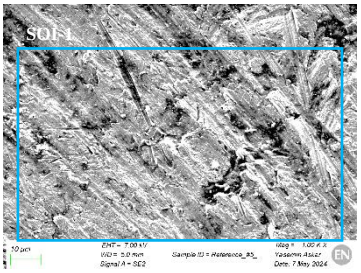	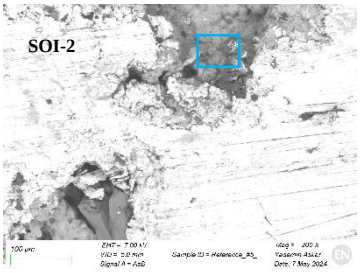

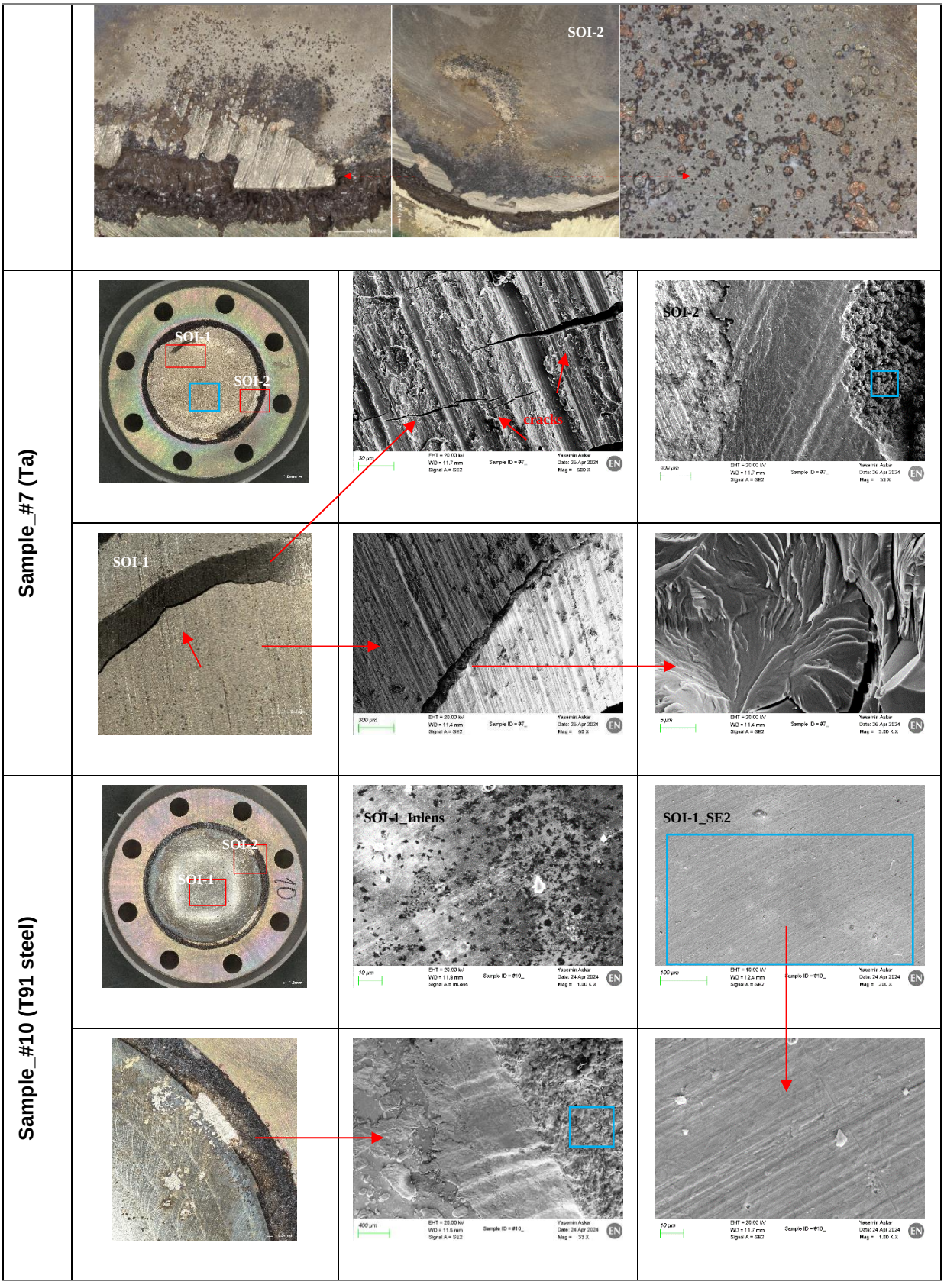
SOI-2
Sample_#7 (Ta)
SOI-1
SOI-2
cracks
SOI-2
SOI-1
Sample_#10 (T91 steel)
SOI-2
SOI-1
SOI-1_Inlens
SOI-1_SE2

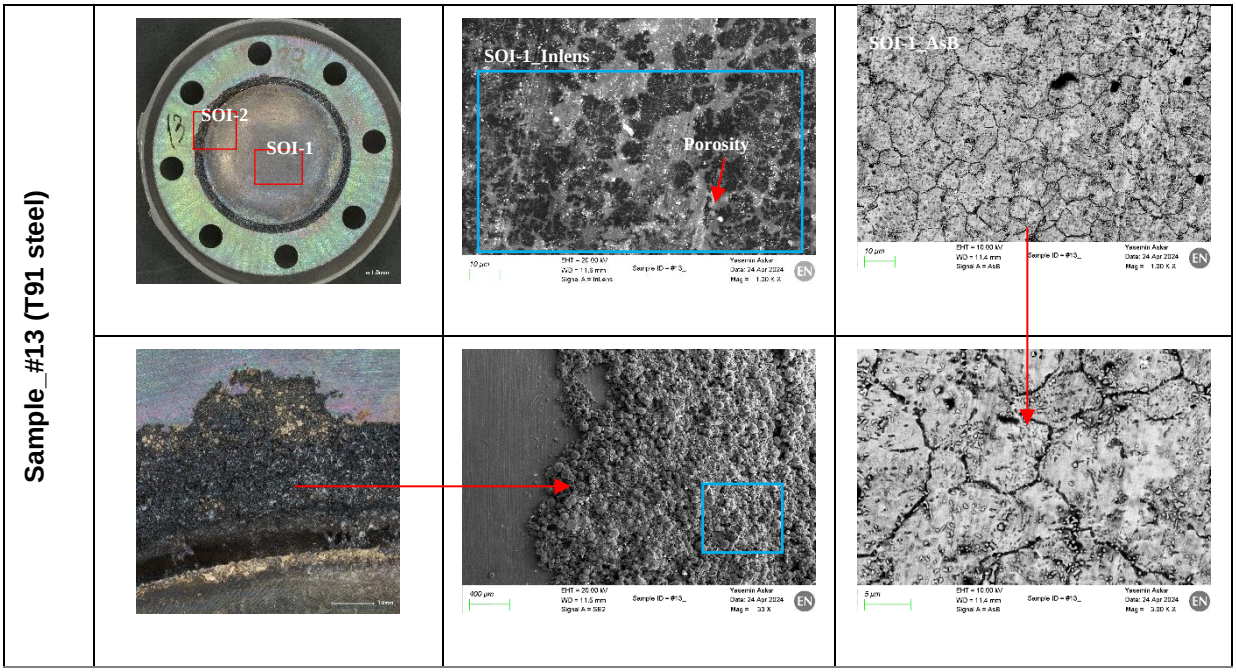

Figure 27: Summary of main observations on samples.

As a summary, the microscopy confirms and further refines the results of the micro-tomography. In a nutshell, it confirms that traces and defects related to the brazing process are visible in most of the samples, strengthening the case for an optimization of this bonding technique. Also, we can detect differences in the material micro-structure at the location of the beam irradiation spot, even though they do not appear very dramatic.

4.4 ELECTRICAL CONDUCTIVITY

Electrical conductivity is not a property of particular interest for beam windows. Usually, such components do not have special electrical requirements. However, measuring electrical conductivity in a non-destructive way is typically much easier than measuring an important property for beam windows such as thermal conductivity. After measuring electrical conductivity, thermal conductivity, in the case of metals, can then be calculated via the Wiedemann-Franz law. This test was in other words an indirect measurement of thermal conductivity.

Two methods were used for this measurement on unirradiated and irradiated samples: the SIGMATEST probe and the four-probe method. The SIGMATEST technique, in fact, although very easy and rapid, can only be used for non-ferrous materials: in this case, for the tantalum samples. For T91 steel, another approach is used, the four-probe method.

The SIGMATEST is a portable eddy current instrument that measures the electrical conductivity of non-ferromagnetic metals based on the complex impedance of the measuring probe. It features five different excitation frequencies and extremely high measuring accuracy. The unit retains this high level of accuracy even at a high frequency of 960 kHz, making it possible to measure very thin workpieces with great precision. In this case, the highest frequency was used. The measuring instrument can automatically standardize the measured value of electrical conductivity to 20°C due

to integrated temperature compensation. The measurement was taken at five different points (see Figure 28).

Figure 28: Samples electrical conductivity, before and after irradiation, was measured at five points using the SIGMATEST.

The four-probe method is the most common technique used for measuring resistance. This technique involves using four equally spaced collinear probes to make electrical contact with the material. Imposing a given voltage to the sample, and measuring the current, it is possible to calculate the electrical resistance, and thus resistivity and conductivity, via the Ohm's law. This measurement is more problematic than the SIGMATEST, given the relatively small size of the samples, which reduces a lot the distance between the four measuring probes. The measurement was taken in two positions, as shown in the Figure 29.

Figure 29: Two positions where the measurements are done using the 4-probe method.

Results for the unirradiated and the irradiated samples are reported in Table 8.

Table 8: Comparison between the electrical conductivity values of irradiated and non-irradiated Ta and T91 steel

Sample number	Foil material	Irradiated sample	Average value of electrical conductivity [MS/m]	Method used for the measurement
Sample #2	Tantalum	NO	7.38	Sigmatest
Sample #4	Tantalum	NO	6.05	Sigmatest
Sample #7	Tantalum	YES	UNSUCCESSFUL	Sigmatest, Four probe
Sample #15	Tantalum	YES	8.17	Sigmatest
Sample #5	T91 steel	NO	1.7	Four probe
Sample #12	T91 steel	NO	1.6	Four probe
Sample #13	T91 steel	YES	1.89	Four probe
Sample #10	T91 steel	YES	2.07	Four probe

On Sample #7, the electrical conductivity measurement failed, independently of the method used, very likely for the strong curvature of the foil. However, as we have seen in section 3, the level of DPA and gas production is the same in the samples of the same material, independently on their thickness. This means that, for tantalum, although statistics is reduced, one irradiated sample can still be taken as a reference for this task.

Surprisingly, the electrical conductivity of both materials seems to be increasing after irradiation. This is not something documented by literature concerning metallic materials, especially considering that no annealing occurs in the samples. In fact, the IRRAD beam is pulsed, and the average energy over time is so small that the expected increase in temperature during irradiation is in the order of a fraction of degree Celsius. In fact, at a second look, we can observe that the apparent increase in electrical conductivity is in the order of the variance of this property in the assemblies, as can be observed when comparing the unirradiated samples (for example, for tantalum, there is a difference of more than 1 MS/m between two samples that are in the same conditions and state).

What we can certainly conclude is that the samples do not experience an observable decrease in electrical (and thus thermal) conductivity after irradiation. This result is very positive. The increase of this property after beam irradiation, on the other hands, is very likely more apparent than real.

4.5 THERMAL CONDUCTIVITY

The Wiedemann-Franz law allows deriving, at a given temperature, the thermal conductivity of a metal out of its electrical conductivity (and vice-versa). It is expressed as:

$$k = \sigma \cdot L \cdot T$$

Where k is the thermal conductivity, σ the electrical conductivity, L the Lorentz number ($2.44 \cdot 10^{-8}\, V^2/K^2$) and T the temperature. The results are reported in Table 9.

Table 9: Comparison between the thermal conductivity values of irradiated and non-irradiated Ta and T91 steel

Sample number	Foil material	Irradiated sample	Average value of thermal conductivity [W/(m K)
Sample #2	Tantalum	NO	54.0
Sample #4	Tantalum	NO	44.3
Sample #7	Tantalum	YES	UNSUCCESSFUL
Sample #15	Tantalum	YES	59.8
Sample #5	T91 steel	NO	12.4
Sample #12	T91 steel	NO	11.7
Sample #13	T91 steel	YES	13.8
Sample #10	T91 steel	YES	15.2

5 Conclusions and future plans

Deliverable D4.3 required the production and testing of two beam window prototypes. With this scope, we have instead produced 8 assemblies, 4 of which were kept unirradiated to be used as

reference for the irradiated samples. The four irradiated samples, made of a stainless steel flange brazed with a metallic foil (tantalum and T91 were identified already during the milestone MS13 as promising candidates as window foils), were irradiated in fall 2023 at the CERN IRRAD facility, with proton beams. After six months of cooldown, the samples were analysed at CERN premises. Results show essentially that:

a. The brazing foil to window needs improvement, as already unirradiated samples show brazing defects and, in 30% of the cases, vacuum leaks even in pristine conditions. This will be in the scope of the remaining work of the task in 2024 and 2025.
b. The concavity / convexity induced by the brazing on the foil is not necessarily a drawback, as better resistance to vacuum pressure can be ensured with a given curvature. What needs to be done is to control the process, with the target of ensuring repeatability of the shape over large series productions.
c. The beam windows show, microscopically, traces of the irradiation, highlighted both by tomography and by microscopy results.
d. However, the macroscopic effect on the thermophysical properties looks to be negligible, as thermal and electrical conductivity maintain the pre-irradiation levels (if anything, we even observe a slight increase in such properties, even though this seems to be related to the variance of this parameter across the samples).

Future work in task 4.3 before the end of IFAST include:

1. Irradiation of additional 4 assemblies at IRRAD with a 5 times higher dose, including this time also a 1 micron thickness graphenic window. This irradiation has already started in April 2024 and will continue until autumn. We target DPAs in the order of ~1e-2, to enlarge the range of the research work, looking for potential use in high activation level facilities.
2. Improvement, together with RHP, of the brazing between foils and flanges, or investigation of alternative tightening systems (clamping with gaskets, diffusion bonding, welding, else).
3. Publication of more scientific papers on international journals of the many results obtained so far in the task. We target at least two more papers on top of those already published. For this work, probably more simulation studies will be needed, for example to better quantify the irradiation boundaries (e.g. temperature) which might have an effect, additional to the radiation damage, on the material evolution. A 6-month internship for a student trainee will be opened in the next months of 2024, to execute this task.

6 References

[1]. H. Wang, C. Meng, H. Qu, X. Sun, P. Wang, and D. Zhu, “Primary Study of High-Power Graphene Beam Window”, in 9th International Particle Accelerator Conference, Jun. 2018. doi: 10.18429/JACoW-IPAC2018-MOZGBE3.

[2]. C. Ader, M. Mcgee, L. Nobrega, and E. Voirin, in Proceedings of the 9th International Particle Accelerator Conference, IPAC-2018, Vancouver, BC, Canada (JACoW, Geneva, Switzerland, 2018).

[3]. L. Notari, “Dynamic radiation effects induced by short-pulsed U-ion beams in metallic targets”, Master Thesis, 2022, DOI 10.5281/zenodo.7484054.

[4]. PS-IRRAD Proton Facility, https://ps-irrad.web.cern.ch/ps-irrad/.

[5]. IFAST Milestone MS13, “First characterisation of beam windows materials under thermomechanical load and extended radiation damage”, 2022, https://zenodo.org/record/7457060#.Y-Jp5a2ZNaQ.

[6]. L. Notari, M. Pasquali, F. Carra, M. Losasso, and M. Tomut, “Materials adopted for particle beam windows in relevant experimental facilities”, Phys. Rev. Accel. Beams 27, 024801, 2024, https://journals.aps.org/prab/abstract/10.1103/PhysRevAccelBeams.27.024801.

[7]. F. Ravotti, “Dosimetry Techniques and Radiation Test Facilities for Total Ionizing Dose Testing”, in *IEEE Transactions on Nuclear Science*, vol. 65, no. 8, pp. 1440-1464, Aug. 2018, doi: 10.1109/TNS.2018.2829864.

[8]. D. E. Groom, N. V. Mokhov, S. I. Striganov, “Muon stopping power and range tables 10 MeV – 100 TeV”, Atomic Data and Nuclear Data Tables, Volume 78, Issue 2, July 2001, Pages 183-356, https://doi.org/10.1006/adnd.2001.0861.

[9]. https://fluka.cern.

[10]. C. Ahdida et al., “New Capabilities of the FLUKA Multi-Purpose Code”, Frontiers in Physics 9, 788253 (2022).

[11]. G. Battistoni, T. Boehlen, F. Cerutti, P.W. Chin, L.S. Esposito, A. Fassò, A. Ferrari, A. Lechner, A. Empl, A. Mairani, A. Mereghetti, P. Garcia Ortega, J. Ranft, S. Roesler, P.R. Sala, V. Vlachoudis, and G. Smirnov, "Overview of the FLUKA code", Annals of Nuclear Energy 82, 10-18 (2015).

[12]. K. Nordlund., S.J. Zinkle, A.E. Sand, F. Granberg, R.S. Averback, R. Stoller, T. Suzudo, L. Malerba, F. Bonhart, W.J. Webe, F. Willaime, S.L. Duradev, D. Simeone, “Improving atomic displacement and replacement calculations with physically realistic damage models”. Nature Communications Commun 9, 1084 (2018).

[13]. A.Yu. Konobeyev, U. Fischer, Yu.A. Korovin, S.P. Simakov, “Evaluation of effective threshold displacement energies and other data required for the calculation of advanced atomic displacement cross-sections”.

Acknowledgements

The authors want to thank the many people who have participated and supported this work, in non-alphabetic order: M. Losasso, E. Neubauer, M. Pasquali, L. Notari, F. Ravotti, F. Pezzullo, D. Bozzato, A.-T. Perez Fontenla, Y. Askar, K. Buchanan, W. Vollenberg, L. Sito, F. Cerutti, A. Pardons, I. Aviles, A. Porret, A. Hervé, J. Gruber, M. Celuch, A. Bertarelli.

Annex A: drawings (components and assembly)

1. Beam windows flange

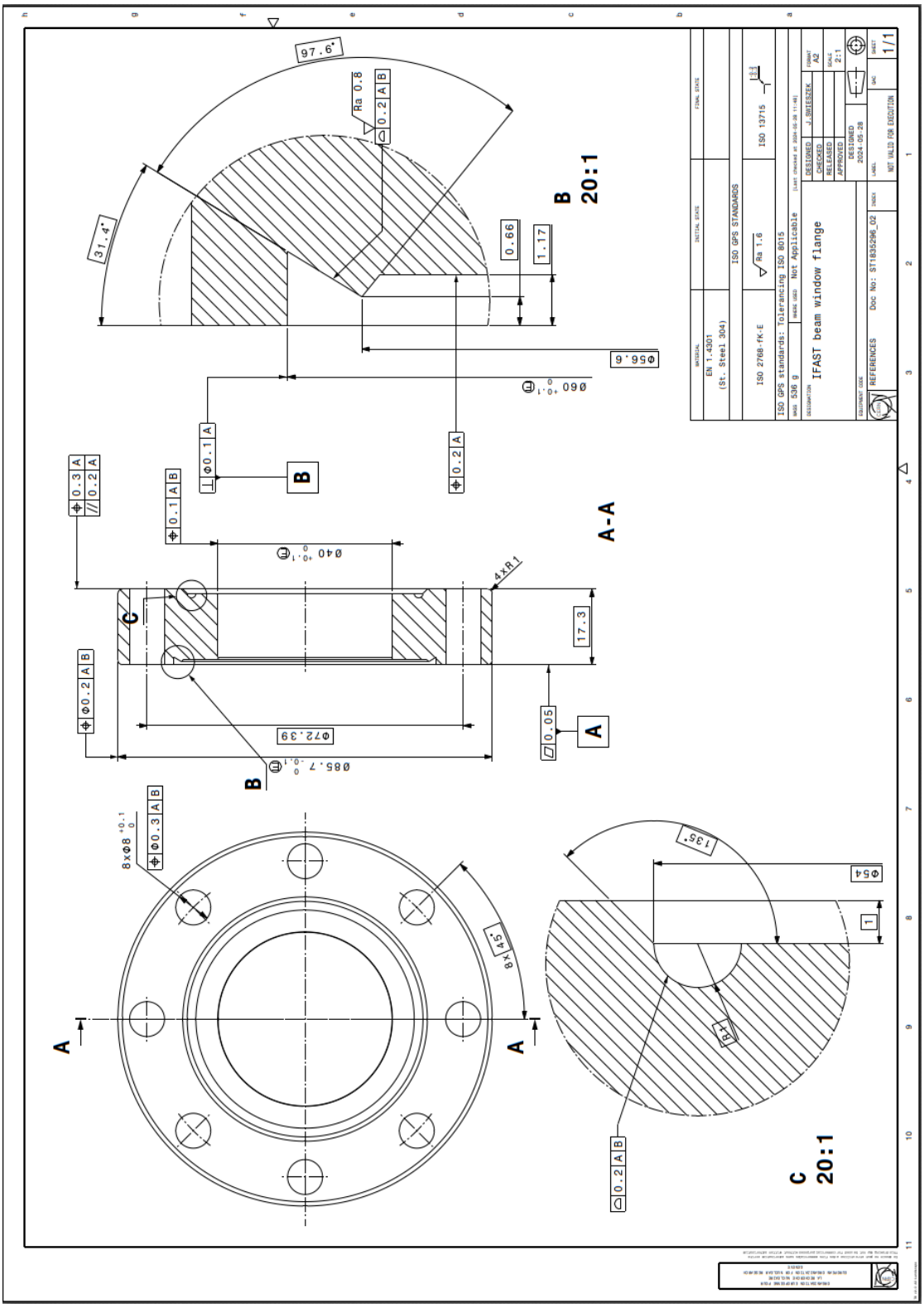

2. Beam windows foil, sample #7

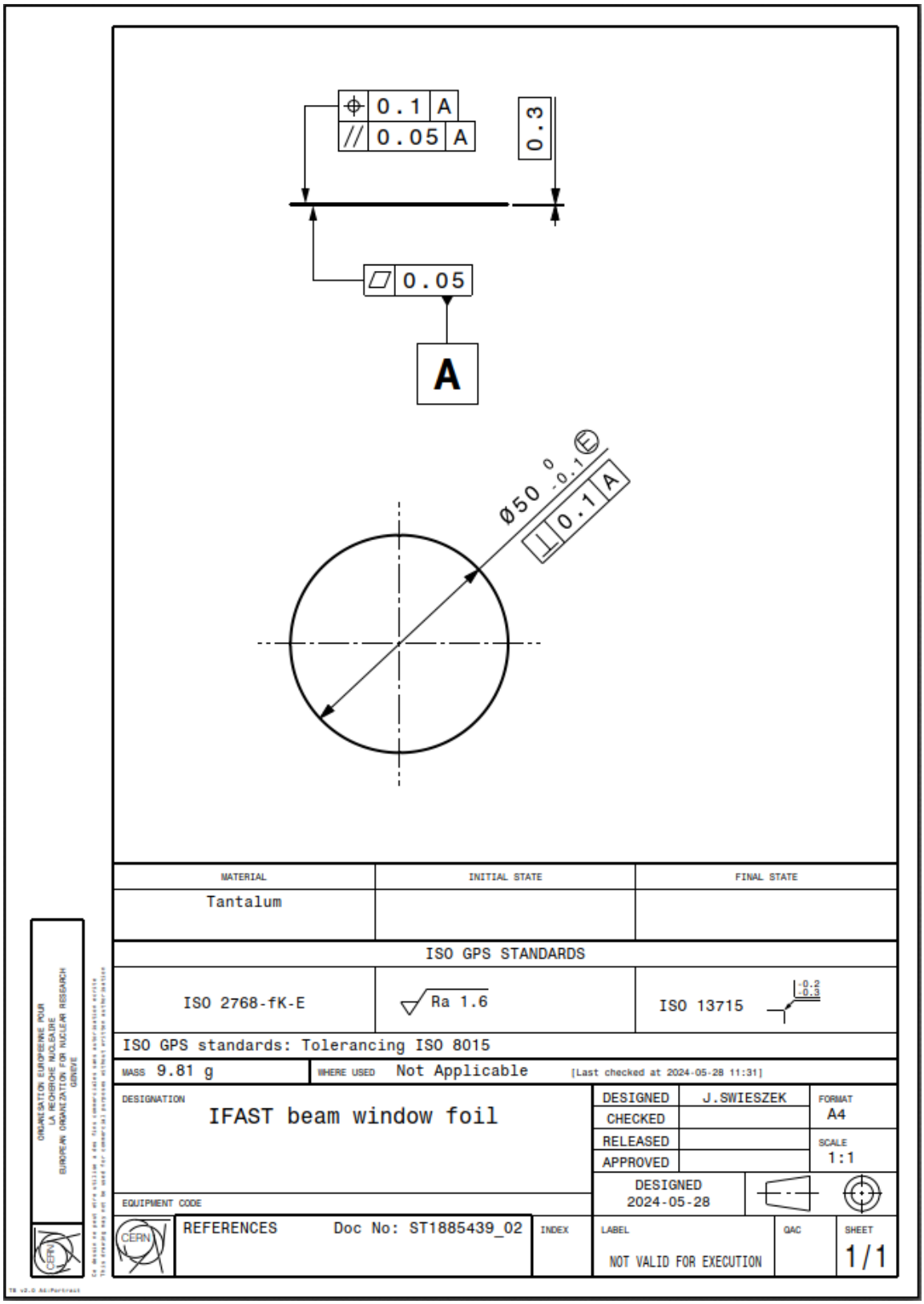

3. Beam windows foil, sample #15

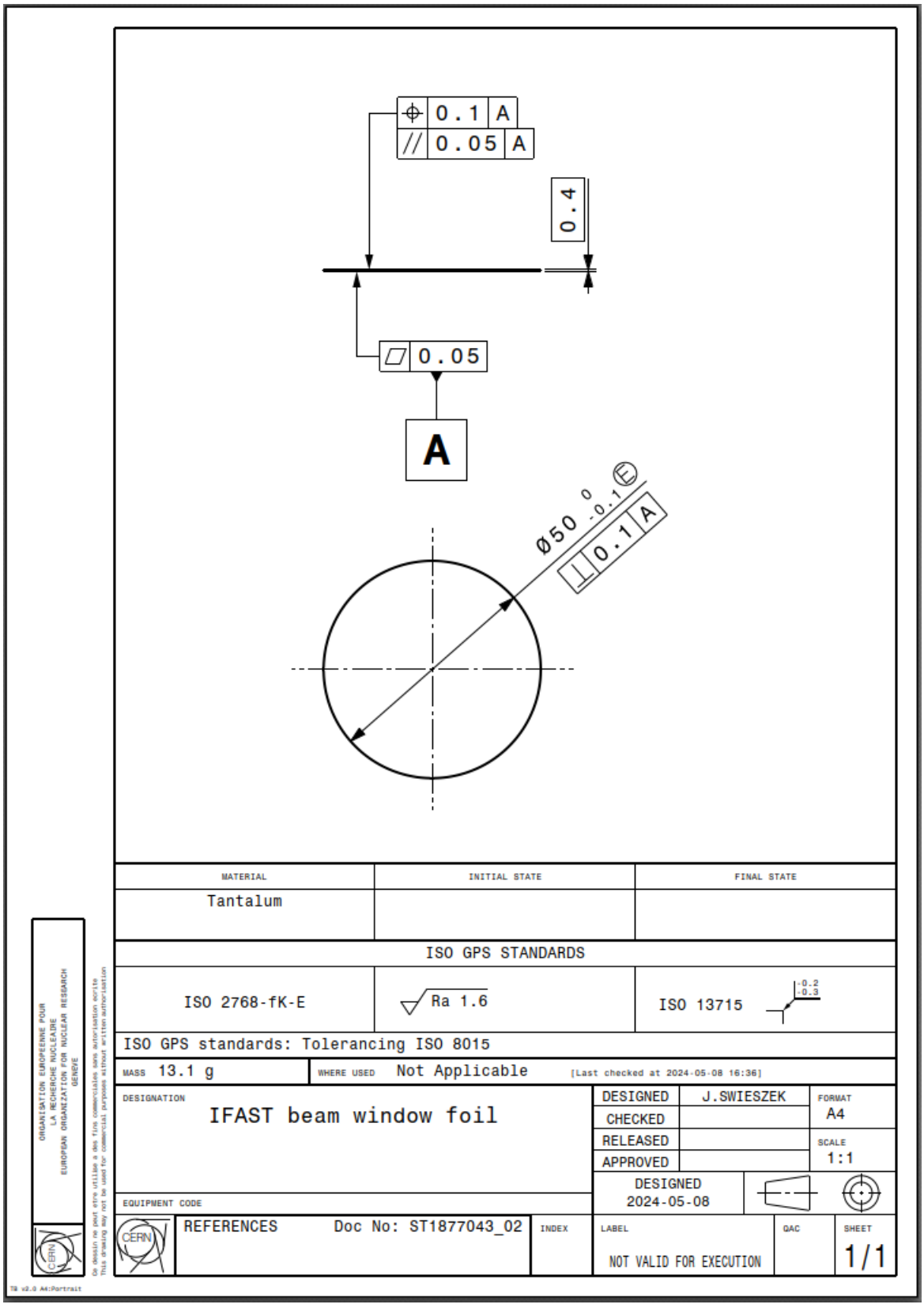

4. Beam windows foil, sample #13

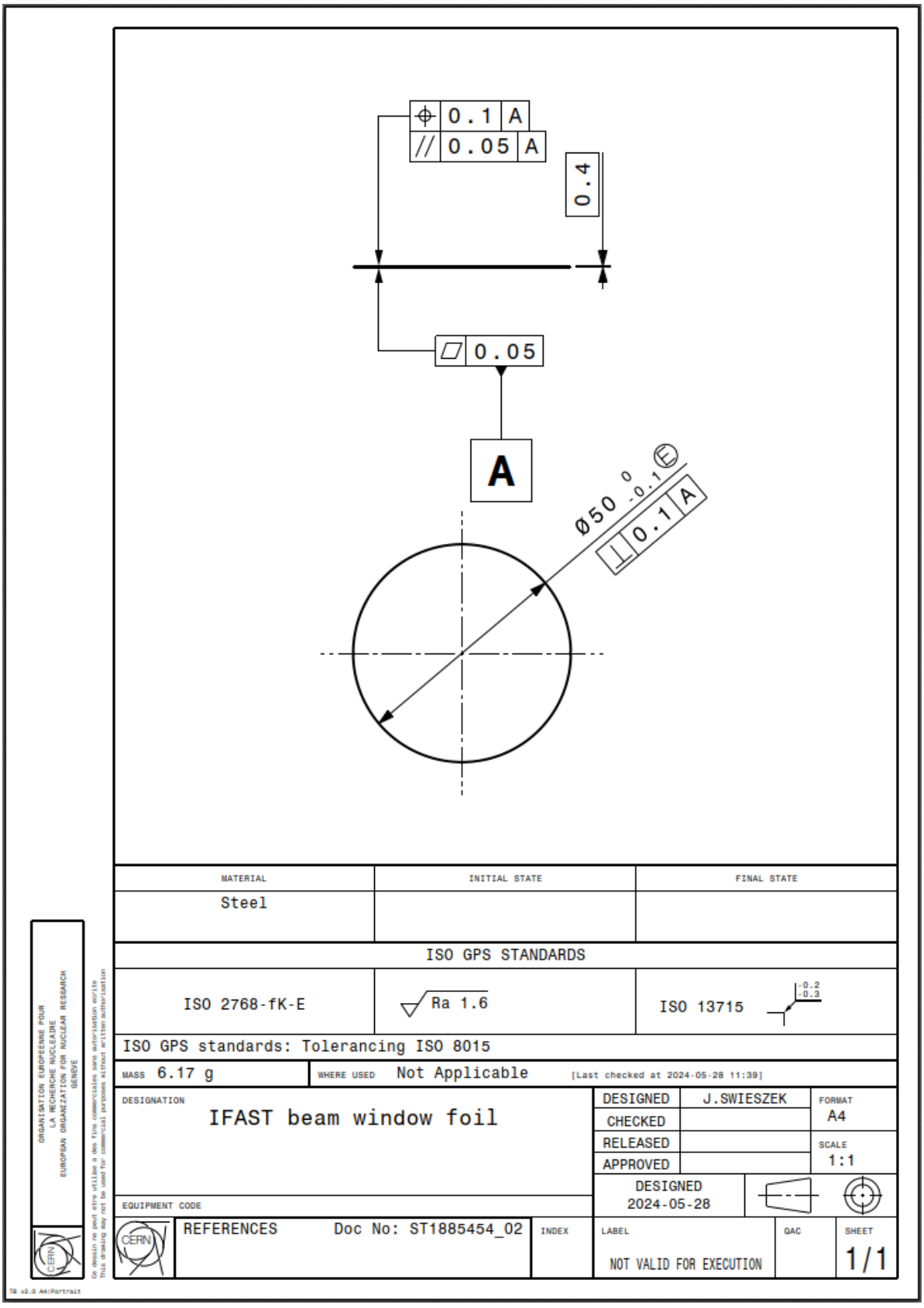

5. Beam windows foil, sample #10

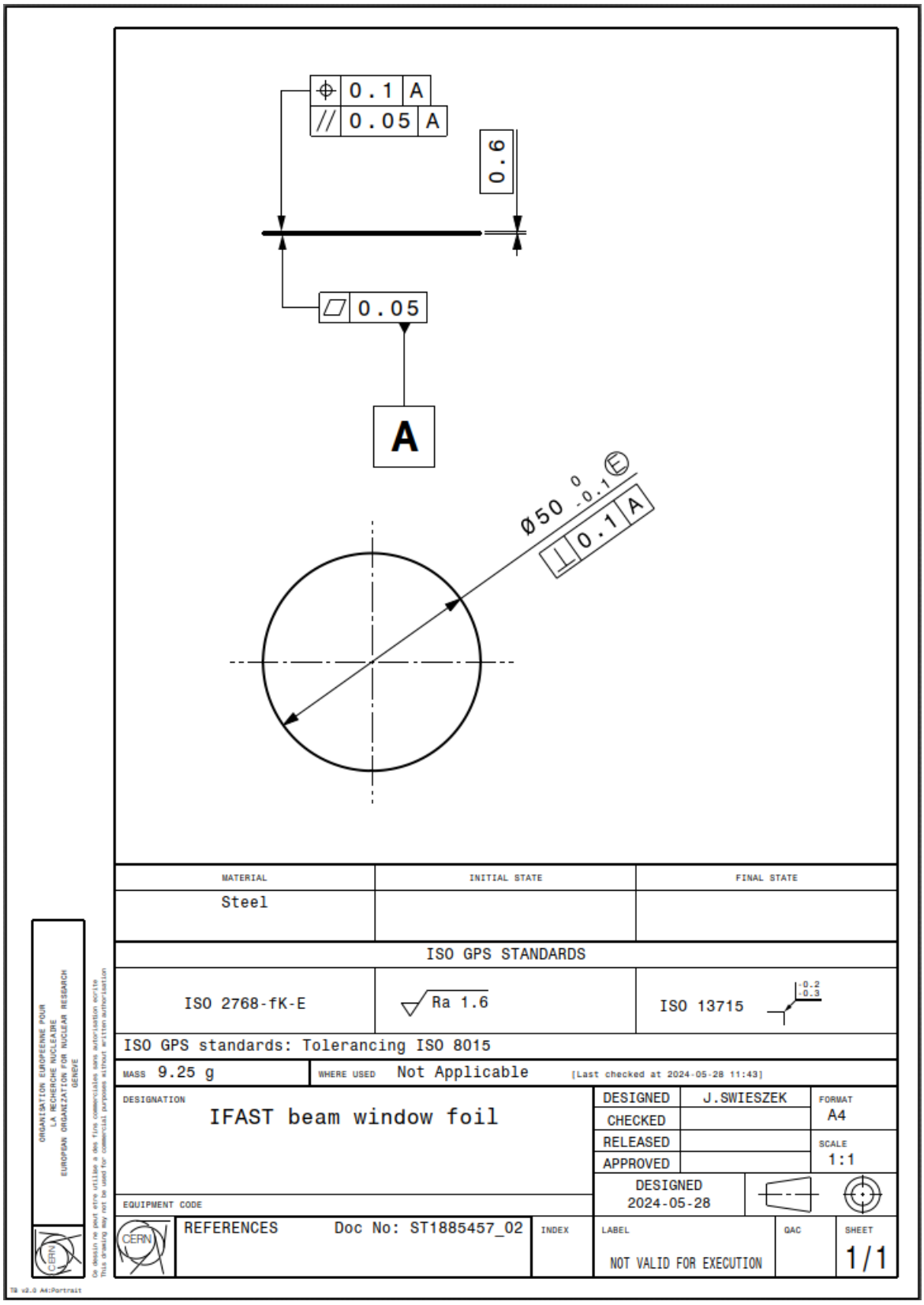

6. **Assembly** drawing